Runaway electrons in tokamaks and their detection using segmented silicon detectors

Master's thesis

Author: **Bc. Sergei Kulkov**

Supervisor: **Ing. Michal Marčišovský, Ph.D.**

Consultant: **Ing. Peter Švihra**

Academic year: **2019/2020**

Katedra: fyziky

Akademický rok: 2019/2020

ZADÁNÍ DIPLOMOVÉ PRÁCE

Student: Bc. Sergei Kulkov

Studijní program: Aplikace přírodních věd

Obor: Fyzika a technika termojaderné fúze

Název práce:
(česky) Ubíhající elektrony v tokamacích a jejich detekce segmentovanými křemíkovými detektory

Název práce:
(anglicky) Runaway electrons in tokamaks and their detection using segmented silicon detectors

Pokyny pro vypracování:

1) Fyzika termojaderné fúze a plazmatu
2) Ubíhající elektrony (RE), jejich vznik v tokamaku, metody diagnostiky a mitigace
3) Dominantní mechanizmy interakce záření s materiálem relevantní k detekci RE
4) Segmentované křemíkové detektory záření pro diagnostiku RE
5) Analýza dat získaných během měření na tokamaku COMPASS

Doporučená literatura:

[1] G. F. Knoll: Radiation Detection and Measurement, Wiley, 2010

[2] G. Lutz: Semiconductor Radiation Detectors, Springer, 1999

[3] P. Kulhánek: Úvod do teorie plazmatu, AGA, 2011

[4] B. N. Breizmann, et al.: Physics of runaway electrons in tokamaks. Nucl. Fusion 59, 083001 (2019)

[5] P. Švihra, et al.: Runaway electrons diagnostics using segmented semiconductor detectors. Fusion Eng. Des. 146, 316 (2019)

Jméno a pracoviště vedoucího diplomové práce:

Ing. Michal Marčišovský, Ph.D., Katedra fyziky, Fakulta jaderná a fyzikálně inženýská ČVUT v Praze

Jméno a pracoviště konzultanta:

Ing. Peter Švihra, Katedra fyziky, Fakulta jaderná a fyzikálně inženýrská ČVUT v Praze

Datum zadání diplomové práce: 25.10.2019

Termín odevzdání diplomové práce: 04.05.2020

Doba platnosti zadání je dva roky od data zadání.

....
garant oboru

....
vedoucí katedry

....
děkan

V Praze dne   25.10.2019

Prohlášení

Prohlašuji, že jsem svou diplomovou práci vypracoval samostatně a použil jsem pouze podklady (literaturu, projekty, SW atd...) uvedené v přiloženém seznamu.

Nemám závažný důvod proti použití tohoto sloního díla ve smyslu § 60 Zákona č. 121/2000 Sb., o právu autorském, o právech souvisejících s právem autorským a o změně některých zákonů (autorský zákon).

V Praze dne..   ....
                                                                        podpis

ii

Název práce: Ubíhající elektrony v tokamacích a jejich detekce segmentovanými křemíkovými detektory
Autor: Bc. Sergei Kulkov

Obor: Fyzika a technika termojaderné fúze
Druh práce: Diplomová práce

Vedoucí práce: Ing. Michal Marčišovský, Ph.D., Katedra fyziky, Fakulta jaderná a fyzikálně inženýrská ČVUT v Praze

Konzultant: Ing. Peter Švihra, Katedra fyziky, Fakulta jaderná a fyzikálně inženýrská ČVUT v Praze

Abstrakt: Relativistické ubíhající elektrony (RE) jsou považovány za nebezpečné v prostředí tokamaků, jelikož nesou velké energie, kterou mohou deponovat v komponentách vakuové komory a poškodit je, pokud nejsou udrženy. Proto je nutno studovat mechanizmy generace RE, hledat způsoby, jak potlačit generace RE nebo zmírnit důsledky jejich kontaktu s komorou tokamaku. Hybridní polovodičové detektory přináší do diagnostiky RE řádu možností a výhod, jako dobré energetické, prostorové a časové rozlišení, radiační odolnost a flexibilitu ve měření díky malým rozměrům. Tato práce shrnuje fyzikální základy generace RE, jejich diagnostiky a mitigace. Dále popisuje fyzikální základy polovodičů, jejich vlastnosti a detektory, které na polovodičích jsou založeny. Nakonec uvádí výsledky z měření hybridním polovodičovým detektorem Timepix3 během jedenácté RE kampaně na tokamaku COMPASS.

Klíčová slova: tokamak, ubíhající elektrony, polovodičové detektory, Timepix3

Title: Runaway electrons in tokamaks and their detection using segmented silicon detectors

Author: Bc. Sergei Kulkov

Abstract: Relativistic runaway electrons (RE) are considered dangerous for the tokamak integrity as they carry significant energy that can be deposited in its chamber components if not confined. Therefore, it is important to study mechanisms of the RE generation, to develop methods, how their generation can be avoided or how their impact can be mitigated. Hybrid semiconductor detectors bring variety of advantages and possibilities to the RE diagnostics. Among them are good energy and spatial resolutions, good radiation hardness, and flexibility in terms of measurements due to their small dimensions. This thesis summarizes physics of the RE generation, methods of diagnostics and mitigation; physics and characteristics of semiconductors and semiconductor detectors. An analysis of measurements conducted with the Timepix3 detector during the 11th RE campaign at the COMPASS tokamak is presented.

Key words: tokamaks, runaway electrons, semiconductor detectors, Timepix3

Acknowledgment

Contents

Introduction

Thermonuclear fusion reactions are the primary source of energy in stars. An immense amount of matter and gravity create a perfect environment for atoms to fuse, releasing energy in the process which powers the stars and defines their lifespan. Thermonuclear fusion is possible on Earth as well. Getting fusion reactions under control is thought to resolve a possible future energy crisis and will bring an effective, lasting source of heat and electric power. However, it is yet to fulfill the expectations vested in it as there are a lot of obstacles to overcome. Fusion energy is still the energy source of tomorrow.

Thermonuclear fusion in a laboratory requires a different approach compared to the stars in order to constrain the reactions and draw energy from them. In fusion experiments, mainly magnetic fields or lasers are used to create conditions when fusion reactions will become possible. Since the late 1960s, tokamaks dominate in the fusion research thanks to the results achieved by over 10 years of experiments starting in 1958. Generally, tokamaks are doughnut-shaped vacuum chambers with magnetic coils around them and the magnetic fields are used to hold the burning plasma, which is a hot medium made of electrons, ions, and neutral particles, and where fusion reactions become possible. The tokamak configuration, which proved to be successful, also has its drawbacks. An interplay between electric and magnetic fields with the plasma is highly complicated and is subjected to a variety of instabilities and processes that tend to stop the fusion reactions. Among them there are the so-called "runaway electrons" which are dangerous for the tokamak vacuum vessel integrity and may compromise the success of the future tokamak experiments and fusion research in general.

Runaway electrons are the electrons which have high, sometimes even relativistic, velocities. In tokamaks, they carry large amount of energy and current and can cause significant damage upon impact with the plasma-facing components. In order to secure the success of the tokamak-based fusion reactors, it is necessary to develop reliable methods of diagnostics, control, and mitigation of the runaway electrons, to study mechanisms of their generation and behavior in the tokamak plasma. Nowadays, nearly every tokamak facility in the world conducts experiments dedicated to the study of the runaway electrons physics. A vast spectrum of different diagnostics is used, via both direct and indirect approach in terms of particle detection. To help resolve the runaway electrons problem, fusion research adapts technology from other branches of experimental physics. Recently, semiconductor detectors, that are commonly used in high-energy particle physics experiments, have found their niche in the fusion research and especially in the study of the runaway electrons physics.

Semiconductor detectors bring a variety of benefits to the plasma diagnostics. Their excellent energy and temporal resolution together with the possibility of separate detection of multiple particles simultaneously gives them an advantage over other diagnostics used in runaway electrons studies. However, semiconductor detectors are still not quite adapted for the tokamak environment and require some time and operation experience to demonstrate their full potential. Nonetheless, the first results acquired during the experiments at the tokamaks are promising.

In this thesis, measurement results with the semiconductor detector Timepix3 conducted at the COM-PASS tokamak during the 11th campaign, which was dedicated to the runaway electrons study, are pre-

sented. The work is composed in the following manner: the first chapter summarizes fundamentals of the thermonuclear fusion, gives a description of the plasma and a tokamak configuration; the second chapter presents a description of the runaway electrons fundamentals, generation mechanisms, methods of diagnostics and mitigation; in the third chapter, mechanisms of the most important (in terms of the runaway electrons detection) interactions between radiation and matter are discussed; the fourth chapter describes semiconductor detectors and principles of operation together with description of the Timepix3 detector; finally, in the fifth chapter, the results obtained with the Timepix3 detector during the experimental campaign are presented. While the most interesting results are discussed in detail in chapter 5, more results can be found in the Appendix. The thesis is accompanied with a list of symbols and acronyms to help with coordination between the chapters.

Chapter 1

Physics of thermonuclear fusion

1.1 Fission and fusion reactions

All chemical elements in our Universe can undergo nuclear transformations, during which new nuclides are produced. This can happen via different reactions between atoms, particles or even within a solitary atom. First, there is nuclear fission, a process when heavy elements split into lighter nuclei either spontaneously or with the help of other particles, such as neutron. Another way for elements to transform is to merge into an atom of an element with a higher atomic number Z. Such a reaction is called a nuclear fusion reaction. Other nuclear reactions include neutron capture, alpha and beta decay, etc [1]. Both fission and fusion reactions obey the laws of physics, mainly mass and energy conservation. However, the twist is that the difference in the mass of the product(s) and the reactant(s) is not zero. That difference takes the form of released or absorbed energy. As well known, mass m and energy E are bound together, as postulated by the famous Einstein relation:

$$E = mc^2,$$ (1.1)

where c is the speed of light. Mass of a nucleus is always different from the sum of the masses of all nucleons inside. These nucleons are kept together by the nuclear force. A measure of this bond is the *binding energy*, which is the minimum energy necessary to break the nucleus into single components - protons and neutrons. The binding energy emerges from the mass difference, which is often called *mass defect*. The binding energy ΔE and the mass defect Δm are connected via similar equation [2]:

$$\Delta E = \Delta mc^2.$$ (1.2)

The energy released or absorbed during fission or fusion reactions is given by the difference of the binding energies of the participant atoms.

Although both fission and fusion reaction may yield energy, the difference in the amount of that energy is quite large. As can be seen in Figure 1.1, the energy per nucleon released as a result of a fusion reaction is significantly larger than from a fission reaction.

In order for fusion and fission reactions to occur, a certain set of conditions must be met. For example, fission reactions may occur for such nuclides as ^{235}U because it is an unstable nuclide: there are too many protons in the nucleus and nuclear forces, which can reach for the neighboring nucleons only at a short distance, are not sufficient to hold the mix of particles together. Repelling Coulomb force, which has far greater reach than nuclear forces, constantly works on tearing the nucleus apart all because of the identical positive electric charge of protons. Fission reactions may occur on its own via radioactive
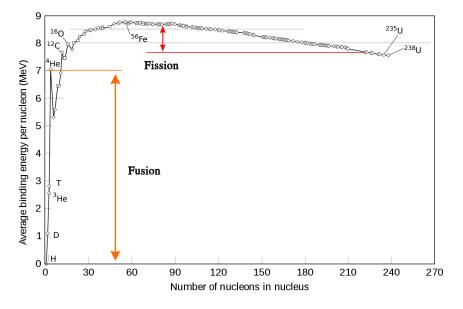
Figure 1.1: The graph of the average binding energy per nucleon as a function of the number of nucleons in a nucleus. The curve is divided by ^{56}Fe into two parts: lighter elements mostly undergo fusion reactions from left to right, heavier - fission reactions (or endothermic fusion reactions in type II supernovae and neutron star mergers). The difference in binding energy for lighter elements, that can be released in a fusion reaction, is shown in orange and the difference for heavier elements in red. The ^{4}He and ^{16}O peaks are linked to the magic numbers 2 and 8. ^{12}C is equal to 3 atoms of doubly magic nuclide ^{4}He which gives it large binding energy per nucleon (this is valid for all elements made of a whole number of ^{4}He atoms except ^{8}Be) [3].

decay or with the help of external particles, i.e., a neutron bombardment which causes changes in the nucleus, forcing it to split. An example of such reaction is one of the reactions of ^{6}Li with neutron n:

$$^6\text{Li} + \text{n} \rightarrow \ ^4\text{He} + \text{T}. \tag{1.3}$$

However, for fusion reactions the situation is opposite. For the nucleons of two different atoms to create a new nucleus, they must overcome the repelling Coulomb force and get to each other so close where nuclear forces can reach. Because of that, fusion reactions are more probable for energetic nuclei. On the other hand, reactions may also occur for nuclei with low energy due to quantum tunneling, when particles penetrate through the Coulomb barrier. One way to give the nuclei sufficient energy is high temperature. As the temperature is a measure of the average kinetic energy of particles, in high temperature environment particles gain large kinetic energy. In that case, one would find himself in the field of *thermonuclear fusion*.

Thermonuclear fusion may be both natural and artificial, controlled, and uncontrolled. Naturally, it occurs in stars, while artificially it was achieved on Earth in the mid 1950s. The first usage of an uncontrolled thermonuclear reaction was utilized in weaponry: thermonuclear, or hydrogen, bombs with fission starter in the form of nuclear bombs and deuterium as a source of extreme energies designed by Edward Teller and Stanislaw Ulam in the 1950s. The first large scale test (known as "Ivy Mike") was conducted in 1952 [4], [5].

In the 1950s, attempts to control thermonuclear fusion reaction as a source of energy were also made though with less luck than in the military applications. In 1951, German-Argentine scientist Ronald Richter together with the president of Argentina Juan Perón claimed, that controlled fusion was achieved

in Argentina [6]. Although it was an overstatement, this has ignited interest in controlled fusion all over the world. This had led to a race between different countries and different machine designs. In 1968 at the conference in Novosibirsk, Russia a winner was set clear: Russian tokamaks T-3 and TM-3 achieved 10 million kelvins in electron temperature [7]. From that day on, almost all bets in the fusion community were on tokamaks, with a stellarator serving as plan B. Tokamaks will be discussed in more detail further in Chapter 1.3.

Almost all chemical elements known to humanity were born in nuclear reactions in stars. While lighter elements up to ^{56}Fe are created in the cores of the stars, heavier elements are born during Type II supernovae, when outer layers of the star are repelled away from the iron-nickel core in an explosion, and neutron star mergers. In this explosion, the matter of the star is bombarded by energetic neutrons and new elements up to uranium are born. However, not everything is born in the stars. It is possible to create super-heavy elements (elements up to $Z = 100$ in the periodic table) bombarding uranium nuclei with neutrons. Furthermore, one can collide heavy nuclei together to create such elements as ^{258}Md and even heavier [8]. More on the evolution of the stars can be found in [9].

Since thermonuclear fusion implies high temperatures, electrons gain enough energy to leave the atom, these reactions occur only in plasma, which is hot gas of ions and electrons.

1.2   Plasma

Plasma is the most common state of the atomic matter in the Universe, as almost all stars, interstellar gases and clouds, and solar winds are made of it. The term "plasma" is used for ionized gas and it was introduced by the American physicist and chemist Irving Langmuir in his article in 1928 [10] because of the similarity between the highly ionized gas and the blood plasma.

Plasma has three key characteristics which distinguish it from solids, gases, and liquids making it the fourth state of matter:

- plasma has free charge carriers - free electrons and ions;

- in plasma, concentrations of negative and positive charges are equal, which is often called quasi-neutrality;

- plasma responds to the electric and magnetic fields as a whole; it can be described as a conductive fluid. Also, plasma can generate those fields by itself.

The second point - quasi-neutrality - does not mean that plasma is completely neutral - it is true only on the large scales. Locally in plasma, electric fields and charged regions can emerge. This can be illustrated via the following model.

Consider a negative and a positive test charges inserted into plasma. Due to Coulomb interaction between the test charges and the bulk plasma, the positive charge will be surrounded by the negative charges (electrons) and the negative - by the positive ones (ions). Each test charge will become screened by the particles of the opposite charge, forming the so-called *Debye spheres*. This is schematically shown in Figure 1.2. Potential of the test particles decreases with distance as $\sim \exp(-\frac{r}{\lambda_{\mathrm{D}}})/r$, where λ_{D} is the radius of the Debye sphere - the *Debye length*, which is defined as:

$$\lambda_{\mathrm{D}} \equiv \left(\frac{\varepsilon_0 k_{\mathrm{B}} T_{\mathrm{e}}}{n_{\mathrm{e}} e^2} \right)^{\frac{1}{2}} , \tag{1.4}$$

where ε_0 is the vacuum permittivity, k_{B} is the Boltzmann constant, T_{e} is the electron temperature, n_{e} is the electron density, and e is the electron charge. The Debye length is a key characteristic of plasma

which offers another explanation of quasi-neutrality. If the size of system containing plasma is larger than the Debye length, then the bulk plasma contains no electric potentials as they are all screened.
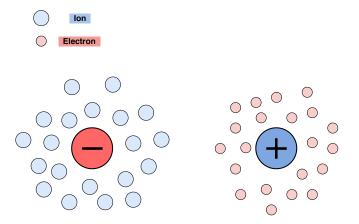

Figure 1.2: 2D representation of a Debye sphere. Test particles put into plasma become screened by the plasma particles of opposite charge.

Another parameter that will be used further in the text is related to collisions, in particular with the Rutherford equation for Coulomb interactions. Consider a collision of two particles of the same charge, the colliding particle α is shifted at distance b (often called *collision parameter*) relatively to the target particle β. The so-called *critical collision parameter* b_0 describes the case when the colliding particle is scattered at a 90° angle and is defined:

$$b_0 \equiv \frac{Q_\alpha Q_\beta}{4\pi\varepsilon_0 \mu g^2}, \ \mu \equiv \frac{m_\alpha m_\beta}{m_\alpha + m_\beta}, \ g \equiv |\mathbf{v}_\alpha - \mathbf{v}_\beta|. \tag{1.5}$$

The collision is shown schematically in Figure 1.3. Collisions in plasma are often considered within the limits. The lower limit is b_0 which describes the collisions at an angle of 90°. The upper limit is the Debye length λ_D which describes the collisions at small angles $\ll 1°$. Using these two parameters one can compare how are the small-angle collisions more frequent than the large-angle ones. The measure of such comparison is the Coulomb logarithm:

$$\ln \Lambda \equiv \ln \frac{\lambda_D}{b_0}. \tag{1.6}$$

1.3 Tokamaks

Attempting to acquire a durable, clear, and safe thermonuclear source of energy, scientists have divided into two groups. Inertial confinement fusion (ICF) is trying to achieve necessary conditions for a fusion reaction in a laboratory use high-power lasers. On the other hand, magnetic confinement fusion (MCF) utilizes the power of super magnets to hold the burning fusion reactions under control. However, scientists at Sandia National Laboratory hope to achieve thermonuclear fusion combining the best ideas from both approaches in their Magnetized Liner Inertial Fusion, also known as MagLIF [11].

Currently, two types of machines lead in the research in MCF: a stellarator and a tokamak. The largest stellarator is the German Wendelstein 7-X, which has achieved positive results during the past
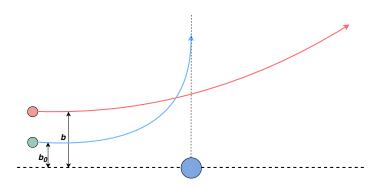
Figure 1.3: Coulomb interaction of particles of the same charge but different collision parameter *b*. Critical collision parameter b_0 describes scattering at a 90° angle.

two years, such as successful divertor operation and pulse length up to 26 s [12], [13]. In stellarators, there is no electric current in plasma which provides greater stability due to the absence of current-driven instabilities. The plasma itself is formed into a twisted shape by a complex vacuum vessel and magnet structure.

Similarly to a stellarator, a tokamak is a machine that exploits the power of magnets to confine hot plasma in a vacuum chamber. However, tokamaks have some unique characteristics. The vacuum chamber made of steel is often shaped in a form of a doughnut, or precisely - torus, with circular or D-shaped cross section. The D-shape of the vessel and magnetic coils helps with keeping more of the plasma volume on the high field side (HFS), which helps with plasma stability. A set of external coils generates a magnetic field in poloidal and toroidal directions with strength up to 12 T [14]. A strong toroidal magnetic field is a key characteristic of a tokamak; its primary purpose is to stabilize plasma and suppress instabilities. The resulting trajectory of plasma particles is a helix, which guides the plasma through both low field side (LFS) and high field side, keeping plasma confined and suppressing particle losses. In the center of the toroidal vacuum vessel is a solenoid, the heart of the tokamak. The primary target of the central solenoid is to induce an electrical current flow through the plasma. It serves as the primary source of energy for plasma, as the electric current generated heats up the fuel via Ohmic heating. However, there are downsides to the central solenoid and electric current flow through the plasma. As the current is generated inductively, a tokamak can sustain plasma only in a pulsed regime. Nonetheless, there are more ways to generate current via current drive, i.e., using Neutral Beam Injection (NBI) and Lower Hybrid Current Drive (LHCD) [15], [16], [17]. On the other hand, electric current in the plasma leads to current-driven instabilities such as kink and sausage instabilities [18]. Also, as plasma heats up, its thermal conductivity rises, making Ohmic heating less and less effective. To make up for the losses in internal heating, tokamaks exploit external power sources, such as NBI, ECRH, and ICRH (Electron and Ion Cyclotron Resonance Heating). The typical tokamak geometry and key components are shown in Figure 1.4.

Isotopes of hydrogen - deuterium and tritium - are often used as a fuel for tokamak plasma. Deuterium-tritium fusion reaction has the largest cross-section for the lowest temperatures. The downside of this reaction is a production of neutrons, which makes the tokamak working with hydrogen isotopes a nuclear machine (neutrons will lead to an activation of the material):

$$D + T \rightarrow {}^4He + n + 17.59 \text{ MeV}. \tag{1.7}$$
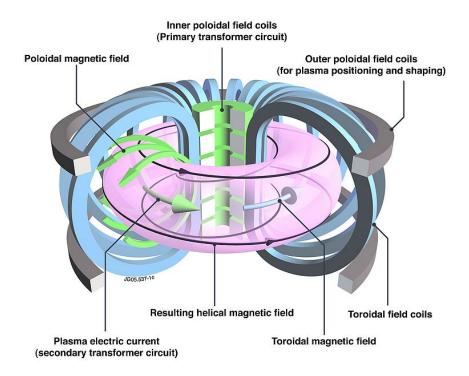
Figure 1.4: The typical tokamak configuration. A primary transformer circuit, or solenoid, is used to generate current in the plasma, poloidal and toroidal field coils are generating magnetic field that shapes the plasma particle flow into a helical trajectory [19].

In the mix of deuterium and tritium, other fusion reaction are also possible [20], such as:

$$D + D \rightarrow \ T + H + 4.03 \text{ MeV}, \tag{1.8}$$

$$D + D \rightarrow \ ^{3}\text{He} + n + 3.27 \text{ MeV}. \tag{1.9}$$

Both reactions have 50% probability. These are the fundamental thermonuclear fusion reactions which will be utilized to generate energy in future fusion power plants. All these reactions yield energy in the form of the kinetic energy of the products. While ions are confined in the magnetic field, neutrons are free to leave the bulk plasma. They collide with the vacuum vessel walls where they release their kinetic energy by heating up the material. Future fusion power plants based on tokamaks will utilize absorbed neutron kinetic energy to produce electricity.

Tritium is an unstable isotope with a half-life of 12.3 years and it is dangerous for a human organism upon inhalation [21]. On the other hand, D-D reaction has lower cross-section (see Figure 1.5). Nonetheless, deuterium is a stable, non-toxic and highly abundant isotope, which can be distilled from water [22]. Tritium is almost absent in nature, but it can be bred from Li:

$$^{6}\text{Li} + n \ \rightarrow \ ^{4}\text{He} + T + 2.75 \text{ MeV}, \tag{1.10}$$

$$^{7}\text{Li} + n \ \rightarrow \ ^{4}\text{He} + T + n - 2.5 \text{ MeV}. \tag{1.11}$$

The first reaction is preferred, as it does not require additional energy. Also, it has larger cross section for low energy neutrons (up to 5 MeV), see Figure 1.6. However, ^{6}Li is quite absent in nature

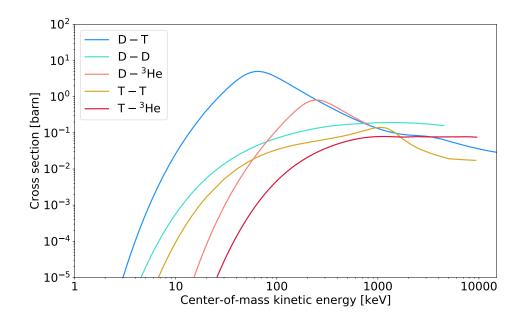Figure 1.5: Cross-sections of different fusion reactions with dependency on center-of-mass kinetic energy. The D-T reaction has the largest cross-section at the low energies. Data taken from [23].

(7.59% abundance on Earth vs 92.41% of ^{7}Li [24]) and it will require enrichment in order to use it in tritium breeders. The most promising compositions of Li that are being tested are lithium-based ceramics Li_4SiO_4 and Li_2TiO_3 [25]. This technology of tritium production will be tested in future experiments at tokamak ITER.

ITER (International Thermonuclear Experimental Reactor) will be the largest tokamak in the world. It is not a power plant, nonetheless, it should bring humanity closer to the utilization of thermonuclear fusion as a source of energy. ITER has many tasks to accomplish. One of them is to produce 500 MW of fusion power in a pulse with a duration exceeding 400 s. Until then the world record belongs to European tokamak JET, which in 1997 produced 16 MW of power [26]. To achieve that, ITER has to successfully control the D-T plasma. Furthermore, ITER aims to demonstrate the feasibility of a vast spectrum of plasma diagnostics, external heating, such as NBI and heating via the electromagnetic waves (ECRH and ICRH), as well as current drive [27], and, in addition, tritium breeding. In the latter stages of ITER experiments, some of the modules of the vacuum vessel's first wall, which faces the plasma, will be exchanged for modules containing lithium creating the so-called *Test Blanket Modules*. Neutrons from the fusion reactions in the plasma will propagate towards the blanket and will interact with lithium producing tritium, which will be later used as a fuel [28]. First plasma in ITER is planned in 2025 [29]. However, there is still a lot of difficulties to overcome. As ITER will be a nuclear installation producing highly energetic neutrons, the machine must withstand high neutron and heat fluxes which damage the plasma-facing components [30]. Another task is to suppress the plasma instabilities, including magnetic islands, MHD and kinetic instabilities [31], to achieve a stable operation and plasma burning. Kinetic instabilities are of particular interest, as they are the source of highly energetic relativistic electrons - the so-called *runaway electrons*, or RE, which can cause damage to the tokamak chamber. The phenomenon of RE will be discussed in more detail in Chapter 2.
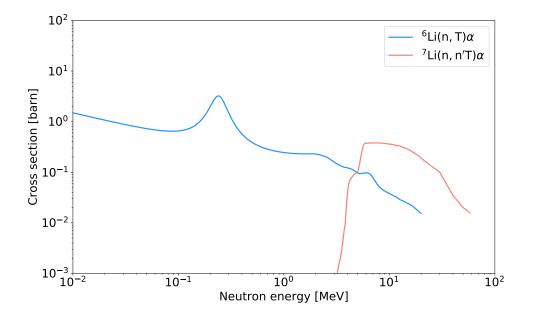
Figure 1.6: Cross sections for two isotopes of lithium with neutrons for tritium breeding. Data taken from [23].

Chapter 2

Runaway electrons

2.1 Runaway electrons fundamentals

Probably the first one who wrote about the possibility of the RE generation in thunderclouds was a Scottish physicist and meteorologist C. T. R. Wilson [32]. Later, REs were discovered during the fusion experiments on tokamaks. Tokamaks generate electric and magnetic fields. Both fields have an effect on the motion of charged particles. Plasma particles - electrons and ions - are gyrating along the magnetic field lines which keeps them confined. The electric field, on the other hand, accelerates the particles. Interchange of energy between the plasma particles is conducted via collisions. Generally, equation of motion for an electron of mass m_e and velocity $v \ll c$ in an electric field may be written in the following form:

$$m_e \frac{d\mathbf{v}}{dt} = \mathbf{F} = \mathbf{F}_e - \mathbf{F}_{drag}, \tag{2.1}$$

where $\mathbf{F}_e$ is the electric force and $\mathbf{F}_{drag}$ is the drag force. These two forces are given:

$$\mathbf{F}_e = -e\mathbf{E}; \quad \mathbf{F}_{drag} = m_e \nu_{coll}(v)\mathbf{v}, \tag{2.2}$$

where $\mathbf{E}$ is the electric field and ν_{coll} is the collision frequency, which depends on the particle velocity and may be written in the following form [33]:

$$\nu_{coll}(v) = \frac{e^4 n_e \ln \Lambda}{4\pi \varepsilon_0^2 m_e^2 v^3}(2 + Z_{eff}), \tag{2.3}$$

where n_e is the electron density, $\ln \Lambda$ is the Coulomb logarithm (1.6), ε_0 is the vacuum permittivity and $Z_{eff} = \frac{\sum_i Z_i^2 n_i}{n_e}$ is the effective ion charge. The factor 2 describes the collisions of the electron with other electrons, Z_{eff} describes the collisions with ions. Dependency of the drag force on the particle velocity is shown in Figure 2.1. Interplay between the drag force and the acceleration by the electric field divides the particle velocity space into three regions, where it is either accelerated by the electric field or decelerated by the drag force. In region I, acceleration by the electric field dominates over the collisional drag force. In region II, balance between the two forces keep particles in the so-called *Ohmic regime*. In region III, particles enter the so-called *runaway regime*, where particles are constantly gaining energy due to acceleration by the electric field reaching relativistic velocities. Since the collision frequency is dependent on the particle velocity as $\nu_{coll} \approx \frac{1}{v^3}$ (or $\nu_{coll} \approx \frac{1}{v^2}$ for relativistic particles), energetic particles are dragged by the collisions less frequently.
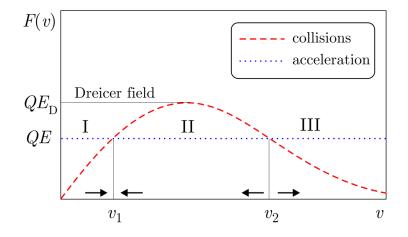
Figure 2.1: Dependency of the drag force on the particle velocity. In the region I, particles are accelerated by the electric field dominating over the drag force. In the region II, particles are trapped in a balancing interplay between the drag force and acceleration by the electric field. In the region III, particles are in a runaway regime, where they are constantly accelerated by the electric field. At the point of $v = v_1$, the drag and electric forces are in a stable equilibrium, at the point $v = v_2$ - in an unstable equilibrium [34].

Comparing the drag force and the electric force

$$F_{\rm e} = -eE = m_{\rm e}\nu_{\rm coll}(v)v = F_{\rm drag},\tag{2.4}$$

one can derive a critical velocity [33]:

$$v_{\rm crit} = \sqrt{\frac{eE}{m_{\rm e}\nu_{\rm coll}}} = \sqrt{\frac{e^3 n_{\rm e}\ln\Lambda(2 + Z_{\rm eff})}{4\pi\varepsilon_0^2 m_{\rm e}E}}.\tag{2.5}$$

Particles with velocities $v > v_{\rm crit}$ are in the runaway regime. The electrons that are in the runaway regime are called *runaway electrons*. If a thermal electron finds itself in an electric field stronger than a critical field (the Dreicer field, more in Chapter 2.2) it will also enter the runaway regime. The generation of REs via acceleration by the electric field is often called *Dreicer mechanism*, and will be discussed in Chapter 2.2.

However, particles are not accelerated until they approach the speed of light: accelerated charged particles are loosing energy via radiation. This is represented in Figure 2.2. On one hand, acceleration by the electric field prevails over the stopping power of collisions and keeps the particles in the RE regime; on the other - particles lose their energy via radiation. Therefore, particles are being trapped in the runaway region. The acceleration is described by the Dreicer mechanism, the radiation losses were derived by Wolfgang Pauli in 1958 [35]. Starting from the Lorentz-Dirac equation of motion, one can derive the radiation reaction force acting on the particle [36]:

$$\mathbf{F}_{\rm rad} = m_0 c\tau_0\left[3\gamma^6(\boldsymbol{\beta}\cdot\dot{\boldsymbol{\beta}})^2\boldsymbol{\beta} + \gamma^4(\boldsymbol{\beta}\cdot\ddot{\boldsymbol{\beta}})\boldsymbol{\beta} + 3\gamma^4(\boldsymbol{\beta}\cdot\dot{\boldsymbol{\beta}})\dot{\boldsymbol{\beta}} + \gamma^2\ddot{\boldsymbol{\beta}}\right],$$

$$\boldsymbol{\beta} = \frac{\mathbf{v}}{c}, \; \gamma = \frac{1}{\sqrt{1 - \frac{v^2}{c^2}}},\tag{2.6}$$
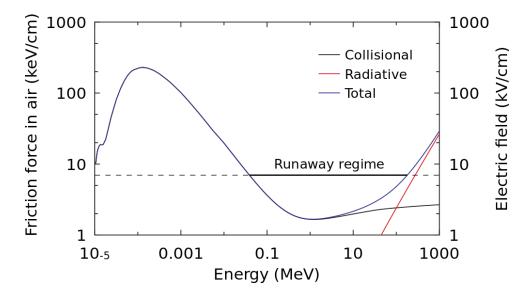
12

Figure 2.2: Representation of the runaway regime. Particles are being pushed into the regime by the electric field. However, radiation losses keep the particles from approaching the speed of light [37].

where m_0 is the particle rest mass, $\tau_0 = \frac{\mu_0 Q}{6\pi c m_0}$ is the so-called *preacceleration time*. Energy loss via particle radiation can be written as:

$$\frac{\mathrm{d}E}{\mathrm{d}t} = m_0 c^2 \tau_0 \left[3\gamma^6 (\boldsymbol{\beta} \cdot \dot{\boldsymbol{\beta}})^2 + \gamma^4 (\boldsymbol{\beta} \cdot \ddot{\boldsymbol{\beta}}) \right]. \tag{2.7}$$

For an electron beam in a tokamak, the complete equation of motion may be written in the following form:

$$\frac{\mathrm{d}\mathbf{p}}{\mathrm{d}t} = \frac{\mathrm{d}}{\mathrm{d}t} (\gamma c m_e \boldsymbol{\beta}) = \mathbf{F}_\mathrm{L} + \mathbf{F}_\mathrm{drag} + \mathbf{F}_\mathrm{rad}, \tag{2.8}$$

where $\mathbf{F}_\mathrm{L} = Q\mathbf{E} + Q\mathbf{v} \times \mathbf{B}$ is the Lorentz force, the radiation reaction is given by the Pauli equation (2.6), and the drag force is defined as:

$$\mathbf{F}_\mathrm{drag} = -\frac{n_e e^4 \ln \Lambda}{2\pi \varepsilon_0^2 m_e c^2} \left[\frac{Z_\mathrm{eff}}{\beta_\mathrm{Ti}^2} \psi \left(\frac{\beta}{\beta_\mathrm{Ti}} \right) + \frac{2}{\beta_\mathrm{Te}^2} \psi \left(\frac{\beta}{\beta_\mathrm{Te}} \right) \right] \frac{\boldsymbol{\beta}}{\beta}, \tag{2.9}$$

where β_Ti and β_Te are the ion and electron thermal velocities, ψ is the Chandrasekhar function [18] defined as:

$$\psi(x) = \frac{2}{\sqrt{\pi} x^2} \int_0^x \xi^2 \mathrm{e}^{-\xi^2} \mathrm{d}\xi. \tag{2.10}$$

2.2 Runaway electrons generation

The RE generation mechanisms can be divided into two groups: the primary and the secondary RE generation. The primary generation - the Dreicer mechanism and the hot tail mechanism - act as a seeding mechanism, as it brings thermal electrons to the RE regime externally, i.e., via acceleration by the electric field or shaping the Maxwell distribution. The secondary one - the avalanche mechanism - multiplies the number of REs by bringing thermal electrons to the runaway regime via collisions,

therefore, REs generate more REs. This chapter describes both types of the RE generation as well as the generation mechanisms in tokamak plasma discharges. Besides the three main mechanisms of the RE generation in tokamaks described further in the text, there are also others, such as β decay, Compton scattering, magnetic reconnection, cosmic radiation, etc. [38], [39].

2.2.1 Primary generation: Dreicer mechanism

Consider an electron moving in plasma with electric field. In the collisional approach, the only mechanism of the electron energy loss is the collisions with other particles. Comparing the acceleration by the electric field and the drag force due to the collisions, one can derive the critical velocity (2.5). From that equation one can derive the critical field also known as the *Dreicer field* which was derived by Harry Dreicer in 1959 [33], [40]:

$$E_\mathrm{D} = \frac{e^3 n_\mathrm{e} \ln \Lambda (2 + Z_\mathrm{eff})}{4\pi\varepsilon_0^2 m_\mathrm{e} v^2}. \tag{2.11}$$

For the electric field with intensity above the critical E_D, all electrons enter the runaway regime. Toroidal electric field in a tokamak is derived as:

$$V_\mathrm{loop} = \oint \mathbf{E} \cdot \mathrm{d}\mathbf{s} \;\rightarrow\; E_\mathrm{tor} = \frac{V_\mathrm{loop}}{2\pi R}, \tag{2.12}$$

where V_loop is the loop voltage in tokamak, E_tor is the toroidal electric field, and R is the major radius of the tokamak (distance from the center of the torus to the center of cross section). The relation between the toroidal electric field and the Dreicer field define the effectiveness of the Dreicer mechanism.

However, equation (2.11) is derived with an assumption that electrons lose energy only via collisions and it is valid only for nonrelativistic case. With the full relativistic approach, one can derive the so-called Connor-Hastie field [41]:

$$E_\mathrm{CH} = \frac{e^3 n_\mathrm{e} \ln \Lambda (2 + Z_\mathrm{eff})}{4\pi\varepsilon_0^2 m_\mathrm{e} c^2}. \tag{2.13}$$

This approximation is valid only for the case of collisional losses of electron energy. Assuming an approximate value for the Coulomb logarithm $\ln \Lambda \doteq 15$, equation (2.13) for the critical electric field can be written in the following form [42]:

$$E_\mathrm{crit} \cong 0.08 n_{20}, \tag{2.14}$$

where n_{20} is the electron density in units of 10^{-20} m^{-3}.

However, experiments conducted at the FTU (Frascati Tokamak Upgrade) showed, that even for the electric field intensities above the Connor-Hastie critical field, no REs can be detected [43]. It is due to neglecting radiative losses in the classical approach in the RE physics when the only energy loss mechanism is through the collisions with the bulk plasma. Those experiments at the FTU made clear, that also another mechanism of the electron energy loss, via radiation, should be also considered. Depending on the intensity of the magnetic field, the impurity concentration, and the RE beam confinement this mechanism can be either the generation of bremsstrahlung or synchrotron radiation.

No matter the mechanisms through which electrons lose their energy in tokamaks, acceleration by the toroidal electric field is considered to be the primary RE generation mechanism and is often called the Dreicer mechanism.

2.2.2 Primary generation: Hot tail mechanism

Another primary mechanism is the hot tail mechanism. It occurs together with the Dreicer mechanism (and the avalanche mechanism, see Chapter 2.2.3) during the disruptions in tokamaks. A disruption, in general, is a rapid loss of plasma confinement. It is defined as a series of events that lead to a fast plasma cooling during its contact with the first wall. It starts with a thermal quench (TQ, loss of the plasma temperature), followed by a current quench (CQ, loss of the plasma current). TQ can be initiated by a sudden rise in impurity concentration when plasma particles lose energy via scattering on the high Z atoms radiating photons [44]. During ionization, impurity atoms also bring more cold electrons to the plasma, shaping the particle distribution of velocities.

Consider plasma in a tokamak which has Maxwellian distribution of velocities. Particles from the bulk plasma collide more often with each other and the impurity atoms, while electrons with the highest velocities (from the right tail of the distribution) undergo collisions less frequently. During disruptions, when energy loss of the bulk plasma is enhanced, the fastest electrons retain their energy, as the cooling process for them takes longer. These electrons are then more likely to enter the runaway regime with the help of the rising toroidal electric field.

As plasma loses energy via radiation, the temperature decreases, which leads to a loss of plasma conductivity [18]:

$$\sigma \sim T_e^{\frac{3}{2}}.$$
(2.15)

Loss of the plasma conductivity affects the current density in plasma $\mathbf{j}$ (Ohm's law):

$$\mathbf{j} = -\sigma \nabla \phi,$$
(2.16)

where ϕ is the electric field potential. Lower current density leads to a more intense toroidal electric field, which can be derived from the Maxwell equations:

$$\nabla \times \mathbf{H} = \mathbf{j}, \quad -\frac{\partial \mathbf{B}}{\partial t} = \nabla \times \mathbf{E},$$
(2.17)

where $\mathbf{H}$ is magnetic field intensity. The Maxwell's displacement current $\frac{\partial \mathbf{D}}{\partial t}$ is neglected due to high conductivity of the tokamak plasmas [18].

At ITER, the hot tail mechanism may dominate the RE generation over the Dreicer mechanism during disruptions. Nonetheless, an increase of the electric field intensity also enhances the Dreicer mechanism. More on the hot tail mechanism of the RE generation can be found in, e.g., [38], [45].
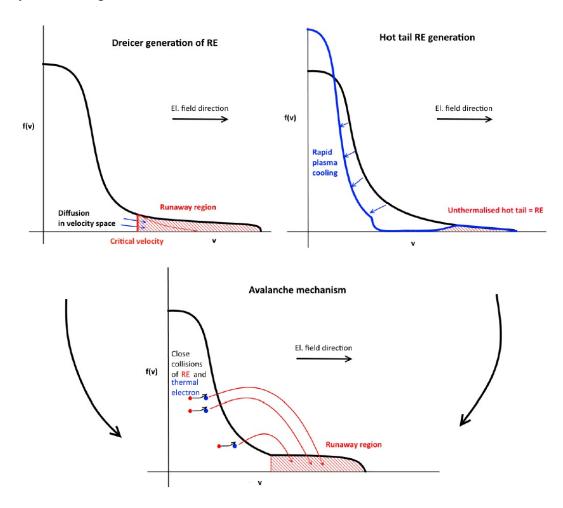
2.2.3 Secondary generation: avalanche mechanism
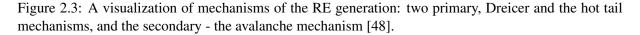
Both primary mechanisms of the RE generation act as a RE seeding, as they are the source of the REs in tokamaks. However, REs may be multiplied in numbers via the so-called *avalanche mechanism*. It occurs only in plasmas where REs are already present.

Although the collision rate of the REs with the bulk plasma is not as high as for the thermal electrons, nonetheless, it does not keep the REs from interacting with other particles. During collisions, REs transfer some of their energy to thermal electrons, and with high enough energy transferred, thermal electrons can enter the runaway regime. Acceleration by the electric field dominates over the collisional and radiational losses which gives the new RE electrons more energy. Furthermore, these electrons may bring more thermal electrons to the runaway regime repeating the whole process. The analytical description of the avalanche mechanism was first given by M. Rosenbluth and S. Putvinski in 1997 [46].

The avalanche mechanism can occur during either a disruption or the flat-top phase of the discharge. In the latter case, the secondary mechanism may become dominant if the flat-top phase is long enough [47].

All three mechanisms of the RE generation - the Dreicer, the hot tail, and the avalanche - are schematically shown in Figure 2.3.

Figure 2.3: A visualization of mechanisms of the RE generation: two primary, Dreicer and the hot tail mechanisms, and the secondary - the avalanche mechanism [48].

2.2.4 Runaway electrons generation in tokamak discharges

A standard tokamak discharge can be divided into three stages: current ramp-up, flat-top, and current ramp-down or, in extreme cases, disruption.

During the plasma breakdown phase, electrons in a partially ionized gas may achieve energies near or above the critical field (2.13). Consequently, these electrons may enter the runaway regime [49]. RE production rate at the early stages of the tokamak discharges is heavily dependent on the impurity concentration in the vacuum vessel. The impurities enhance plasma cooling, which with high collision rates of the electrons with the impurities itself lowers the plasma conductivity leading to a rise in the loop voltage. This effect takes the toroidal electric field (2.12) value closer to the critical electric field.

Nonetheless, RE generation in the early stages of the discharge can be suppressed via specific fueling scenarios [50].

RE generation during the flat-top phase was studied in the experiments at FTU, DIII-D, and TEXTOR tokamaks during a joint ITPA (International Tokamak Physics Activity) campaign [42]. Though the primary target of the campaign was to measure the actual critical electric field value, considering other RE energy loss mechanisms than just the collisional losses, it was chosen to achieve RE generation in the flat-top phase, when the plasma parameters are held constant. These experiments have shown, that the plasma density is probably the key parameter that affects the RE production rates during the flat-top phase. Discharges with the same loop voltage V_{loop} but different plasma densities will have a different amount of the REs generated. The result is shown in Figure 2.4. These experiments prove, that in order to avoid or at least to suppress the RE generation during the flat-top phase, it is sufficient to hold the plasma density at such levels, that the toroidal electric field is below the critical value.
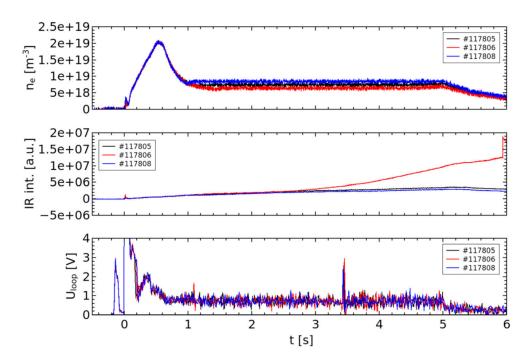
Figure 2.4: Three different discharges at the TEXTOR tokamak with the same parameters except plasma density, which was held constant for the most part of the discharge. The experiment has shown, what effect has a shot-to-shot different plasma density on the RE production rates (graph in the center, infrared signal from the RE synchrotron radiation) [42].

In the discharges that terminate with a current ramp-down, REs are not considered a problem as they are either confined of can be easily mitigated. On the other hand, discharges that are terminated in a disruption are considered the most dangerous in terms of the RE generation. Post-disruption RE generation may arise through the both Dreicer and hot-tail mechanisms (and through other mechanisms, such as Compton scattering [51]) and further multiply in number via the avalanche mechanism because of the induced toroidal electric field following a CQ, and enhanced plasma cooling due to high-Z impurities [52], [53], [45], [54]. These REs then can form a RE beam that can carry up to 80 % of the pre-disruption plasma current [55]. If such RE beams will survive long enough, they will form a so-called *RE plateau*. There are multiple ways to enhance the RE energy loss and thus mitigate their impact on tokamak structures. This will be discussed in more detail in Chapter 2.4.

2.3 Runaway electrons diagnostics

REs are considered dangerous for the tokamak operation, especially the REs generated in disruptions [46], [56], [57]. Therefore, in order to secure the successful operation of the future machines such as ITER, it is important to develop reliable RE diagnostics and strategies for their mitigation. This chapter will summarize the majority of the diagnostics used in the RE research. Physical processes, relevant for the radiation and neutron diagnostics during the experiments dedicated to studying the RE physics, are discussed in Chapter 3.

REs in tokamaks (as charged particles put into electric and magnetic fields) constantly radiate photons either through synchrotron radiation (contained RE beams) or via bremsstrahlung generation (on ions or during the first wall strike by the REs). Relativistic REs radiation is concentrated in a cone along their path. Radiated photons cover a wide spectrum of energies from a few eV to tens of MeV. However, there is no diagnostic that can cover the whole energy spectrum, and generally, the whole scope of the RE diagnostics is quite limited [58], [59], [60], [61].

Depending on the energy, X-ray photons can be divided into two groups: soft X-rays, or SXR, with energies from a few hundreds of eV to 10-20 keV; hard X-rays, or HXR, with energies from 10-20 keV to tens of MeV. For the SXR detection, semiconductor detectors are usually used, while for HXR - scintillation detectors are common [38]. In addition, part of the photons produced by REs are in the visible spectrum, which makes possible detection by fast cameras [62]. Semiconductor detectors will be described in Chapter 4. Fundamentals of scintillation detectors are discussed in [63].

Among the direct RE diagnostics, which measure either radiation generated by the REs or impact of the RE beams, also belong Langmuir and calorimetric probes [64], detection of electron cyclotron emission, or ECE, [65], [66], Cherenkov detectors [67], [68], and infra-red tomography [69], [70]. The RE generation and their evolution in tokamak plasmas can be also studied indirectly via measuring the loop voltage, temperature and density profiles (Thomson scattering), analyzing changes in the plasma current (Rogowski coils), the average plasma density (microwave interferometers), and a vast scope of the magnetic diagnostics (e.g. Mirnov coils). Also, pellet injections have found use in RE research (i.e. location of the RE beam edges) [38].

All diagnostic techniques have their limits. For example, scintillation detectors may provide information about the HXR radiated from the tokamak or neutrons (either fusion or nonfusion, such as photoneutrons). A sufficient lead shielding will cut off the photon signal leaving a separate signal from the measured neutrons. However, the most powerful gamma radiation generated by the REs may penetrate such shielding, leading to a contaminated signal from the scintillation detectors. All detectors that rely either on particle or photon detection may become saturated. On the other hand, all detectors have predefined sensitivity, which means they can generate signals only if the incoming radiation or particle has sufficient energy. This complicates measurements of the early generated REs [42]. Also, usage of shielding leads to a secondary generation of Compton electrons, which then mix up with the radiation signal from the tokamak.

2.4 Runaway electrons mitigation

Because of the danger that REs pose, it is necessary to mitigate their generation and impact on the tokamak structures. As has been discussed in Chapter 2.2.4, it is rather easy to avoid RE generation or suppress REs in the early stages of the discharge via an appropriate fueling scenario. The current flat-top phase is safe against RE production because of the high fusion-relevant plasma density [71]. On the other hand, post-disruption REs are a serious threat to the vacuum vessel integrity if not confined or mitigated properly. Besides the RE generation, disruptions are also unfavorable for the tokamak operation, since

they lead to high heat fluxes onto the first wall and large electromagnetic load to the steel structures and magnetic coils due to the halo currents [72]. These undesirable effects may sabotage the successful operation of the larger machines, such as ITER. To secure the success of future experiments, a so-called *Disruption Mitigation System*, or DMS, is being developed for ITER [73].

RE generation avoidance was given top priority for ITER DMS [74]. This is planned to be achieved via injections of hydrogen or deuterium (fusion fuel) mixtures with high-Z noble gases, such as Ne or Ar. If RE generation has not been avoided, the second step is to enhance the RE energy dissipation via radiation. This can be accomplished in two different ways: massive gas injection (MGI) or shattered pellet injection (SPI) in the current quench stage of the disruption [38], [52], [74]. The main idea behind the massive material injection is to stimulate the isotropic distribution of the RE energy, rather than local in the case of first wall strike [51]. MGI has been already successfully tested at tokamak JET with the ITER-like wall [75]. However, SPI tests on the DIII-D tokamak showed that SPI has greater penetration than MGI [76]. Both MGI and SPI systems are under preparations for the ITER DMS. However, there are still open questions considering MGI and SPI systems that require further research [47].

There are other approaches in RE mitigation being studied at different machines. For example: non-axisymmetric fields [71], [77], [78], RE plateau control [79], [80]. However, these are out of consideration for ITER DMS [74].

Chapter 3

Interaction of radiation with matter

This chapter discusses the most important physical processes of the photon-matter interaction on which RE diagnostics rely. REs lose their energy via interactions with both the bulk plasma and the tokamak first wall. It is important to understand photon-matter interactions to prepare the right diagnostic. In addition, neutrons can also provide information about the REs.

3.1 Runaway electrons energy loss via radiation

Generation of bremsstrahlung and synchrotron radiation are the major mechanisms of the RE energy loss in tokamaks. Bremsstrahlung is electromagnetic radiation produced during a Coulomb interaction between two charged particles. In tokamak plasma, REs are constantly scattered on the particles of the bulk plasma. However, if REs leave the plasma, they impact onto the first wall where they deposit their energy heating up the material. The REs that generated bremsstrahlung in plasma continue in their way with lower energy, while the REs that hit the wall are stopped by the material. In both cases, the bremsstrahlung spectrum is continuous with energies even up to kinetic energy of the parental electron in the case of the RE-wall interaction. The generation of bremsstrahlung is schematically shown in Figure 3.1.

Interaction of REs with ions dominates over the repelling by the bulk plasma electrons due to larger mass and lower velocity of the ions. Consider an electron scattering on an ion. Equation of motion of the electron will be:

$$m_e \ddot{r}_e = \frac{Ze^2}{4\pi\varepsilon_0 r_e^2},$$ (3.1)

where the right side is the Coulomb force and Z is the ion atomic number. The electron electric dipole moment will be:

$$\mathbf{p}_E = e\mathbf{r}_e, \ \ddot{p}_E = e\ddot{r}_e = \frac{Ze^3}{4\pi\varepsilon_0 r_e^2 m_e}.$$ (3.2)

Combining the equation above with the Larmor formula:

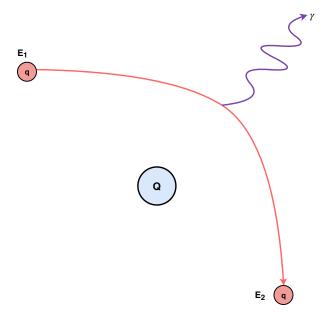$$P_{br} = \frac{\ddot{p}_E^2}{6\pi\varepsilon_0 c^3},$$ (3.3)

Figure 3.1: Emission of bremsstrahlung during the Coulomb interaction of two particles. A photon of energy $h\nu = E_1 - E_2$ is generated by the incident particle. Some momentum would be also transferred to the particle with charge Q.

one will get the radiated power of the electron via bremsstrahlung [36]:

$$P_{\mathrm{br}} = \frac{Z^2 e^6}{96\pi^3 \varepsilon_0^3 c^3 r_{\mathrm{e}}^4 m_{\mathrm{e}}^2}. \tag{3.4}$$

Power loss of a RE beam via bremsstrahlung from the interactions of REs with ions is given in [31]:

$$P_{\mathrm{br}} = 5.35 \times 10^{-37} Z^2 n_{\mathrm{e}} n_{\mathrm{z}} T_{\mathrm{e}}^{\frac{1}{2}}, \tag{3.5}$$

where n_{z} is the ion density. Generation of bremsstrahlung is more intense in case of heavier ions, which can be impurities in tokamak plasma. This fact can be used to suppress the REs in tokamaks and mitigate their impact onto the first wall. Injecting high Z noble gases (i.e. Xe, Ar) into the RE beam will lead to an intense generation of bremsstrahlung consequently weakening the beam [81]. Measuring the bremsstrahlung photons as a secondary radiation is the general way to learn about the REs energy, interactions and losses.

As particles gyrate along the magnetic field lines, they lose energy via *cyclotron radiation*. Equation of motion of electrons in that case will be:

$$m_{\mathrm{e}} \ddot{r}_{\mathrm{e}} = e v_\perp B, \tag{3.6}$$

where $v_\perp$ is the electron velocity perpendicular to the magnetic field lines. The second time derivation of the electron electric dipole moment then is:

$$\ddot{p}_{\mathrm{E}} = \frac{e^2 v_\perp B}{m_{\mathrm{e}}}, \tag{3.7}$$

and the power loss via cyclotron radiation is [36]:

$$P_{\text{cycl}} = \frac{e^4 v_\perp^2 B^2}{6\pi\varepsilon_0 c^3 m_{\text{e}}^2}. \tag{3.8}$$

However, this does not apply to relativistic electrons which will undergo rather *synchrotron radiation* emission. Dependency on the magnetic field *B* also applies for the synchrotron radiation. More on the synchrotron radiation of the relativistic electrons in tokamaks can be found in [82]. Which one of the two radiation mechanisms prevails - cyclotron (or synchrotron in the case of relativistic electrons) or bremsstrahlung - generally depends on the magnetic field *B* and impurity concentration (Z, n_z). However, in the case of the RE beam impact onto the first wall, bremsstrahlung will be the main power loss mechanism as the beam energy is absorbed by the wall material.

3.2 Photon-matter interactions

The bremsstrahlung photons generated by the RE interactions with the plasma particles or the first wall cover a wide spectrum of energies from a few keV to tens of MeV. These photons are also interacting both with the plasma and the first wall. Depending on the photon energy, photon-matter interactions can be divided into three dominating types: the photoelectric effect, Compton scattering, and pair production.

The photoelectric effect is an emission of electrons by atoms that absorb the incident radiation. Electrons bound to the atom occupy certain energy levels as well as orbits around the nucleus. These electrons can absorb incident photons. If the photon energy is larger than the so-called *ionization energy*, which is the energy required for an electron to leave the atom, the electron after absorbing the photon leaves its orbit with energy $E = h\nu - U_{\text{ion}}$. If the energy is not enough, it pushes the electron to a higher energy level in atom. The atom becomes excited and eventually the electron returns back to its position radiating a photon during the process. The probability of the photoelectric effect is highest for the photons with energies from a few eV to tens of keV, depending on the atomic number *Z* of the target material.

Compton scattering describes the scattering of a photon on an electron. Usually, Compton scattering occurs on electrons that are loosely bound on outer orbits, and to interact with them, photons must have high enough energy $h\nu_{\text{c}}$. For such photons, loosely bound electrons may be considered almost free. During the interaction, the photon changes its direction and passes some of its energy to the electron, continuing with energy $h\nu'$. The electron leaves the atom becoming a so-called *Compton electron* with kinetic energy $E_{\text{kin}} = h\nu_{\text{c}} - h\nu'$. Energy passed to the electron and the direction of the photon and electron after the interaction depends on the scattering angle. Compton scattering dominates for photons with energies from a few keV to a few MeV.

For the most energetic photons, the pair-production mechanism becomes possible. If a photon passing close to a nucleus has energy above 1.022 MeV, which is the energy threshold for production of an electron-positron pair, it may interact with the nucleus transforming its own energy into mass creating an electron and a positron. The process happens in the vicinity of the nucleus to ensure momentum conservation (it may also occur on electrons - triplet production, when two electrons and a positron are generated). The generated particles fly off interacting with the surrounding material. After encountering an electron, the positron annihilates with it producing two photons (or, in the less probable cases, more than two photons), each with energy 0.511 keV [83], [84].

All three processes are schematically shown in Figure 3.2. Which way will the interaction undergo is given by the cross section which depends on the energy of the incident photon and the material atomic number *Z*. For a silicon semiconductor detector, which will be discussed in Chapter 4, cross sections of the photon-matter interactions are shown in Figure 3.3. For the detectors of highly energetic photons, or HXR, a lead shielding is usually used to cut off the low energy photons and get a clear signal.

Bremsstrahlung photons produced by the REs in tokamaks may interact with the shielding producing, i.e., Compton electrons which are further detected as a background by the diagnostic. Cross sections for lead are shown in Figure 3.3.
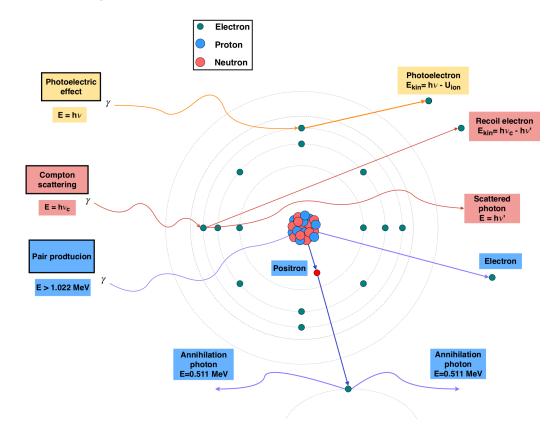
Figure 3.2: The three main mechanisms of photon interaction with matter: the photoelectric effect in yellow, Compton scattering in red, and pair production in blue. Representation of an atom of ^{28}Si.

Figure 3.3: Cross sections of the three dominate mechanism of photon-matter interaction for ^{28}Si (left) and ^{208}Pb (right). Peaks in the probability of photoelectric effect corresponds to K atomic shell for ^{28}Si and M, L and K atomic shells for ^{208}Pb. Data taken from [85].

3.3   Photoneutrons

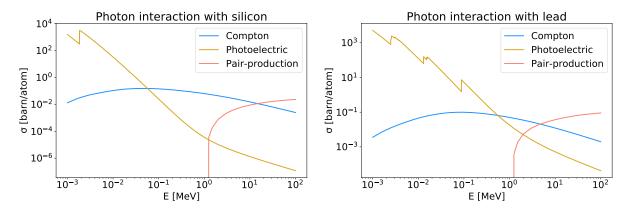Generally, neutrons in tokamaks are produced primarily in reactions such as D-T or D-D. However, in the presence of REs in a tokamak, a new mechanism of neutron generation becomes possible. If REs will get to contact with the first wall (i.e. REs generated after a disruption), they will lose their energy through collisions and radiation. The latter leads to generation of bremsstrahlung photons [86], which can afterwards interact with nuclei, i.e., $^{i}X_j$ producing an element $^{i-1}Y_j$ and a neutron:

$$^{i}X_j + \gamma \rightarrow \, ^{i-1}Y_j + \text{n}. \tag{3.9}$$

Photoneutrons are not generated instantly after a disruption. Instead, REs have to gain some energy depending on the first wall material to satisfy the energy threshold of a photoneutron generation. Nonetheless, during disruptions REs can be accelerated to energies well over 100 MeV [86].

Free neutrons continue their path deeper into the first wall colliding with nuclei. As a neutral particle, neutron does not interact via Coulomb collisions which makes neutron detection more complicated than detection of charged particles. Generally, interactions of photoneutrons and nuclei can be divided into two groups.

Slower neutrons (neutrons with energies up to a few eV) with low energy undergo elastic scattering, and neutron-induced nuclear reactions prevail. The latter can act as a source of secondary radiation due to the neutron capture reactions (n, γ). However, such reactions are not favorable for the neutron diagnostics because photons are difficult to detect. On the other hand, reactions (n, α) and (n, p) produce charged particles that are rather easy to detect.

Faster neutrons are much harder to detect because of the low cross section of photoneutron-nucleus interactions. However, such neutrons lose their energy through a series of scattering interactions, during which neutron passes some of its energy to the surrounding nuclei. In order to stop the neutron, low Z moderators, such as hydrogen rich materials, are used. For fast neutrons, an inelastic scattering can also occur exciting the targeted nucleus which then leads to a photon emission. This gamma radiation contributes to the neutron signal complicating the data analysis.

In tokamaks, a neutron shielding is a key task, since they penetrate deep into the material. Blanket modules in the ITER first wall will provide shielding against neutrons protecting the steel structure and the superconducting magnets [87]. Also, capturing neutrons is the general way to extract energy from the plasma. For example, neutrons from the D-T reaction carry 80% of the energy released (14.1 MeV) [88]. Penetrating through the blanket modules, neutrons from the plasma heat up the surrounding material which is cooled by water. The energy cycle of a thermonuclear fusion power plant is basically the same as the one of a nuclear power plant [89]. Neutrons may also prove useful in production of fusion fuel - tritium - via reactions with ^{6}Li (1.10) and ^{7}Li (1.11). Neutron diagnostics thus provide information about plasma parameters [88] as well as about REs [61], [79].

3.4   Interaction probability

The probability of a photon-matter interaction depends on the photon energy and the material properties. Due to the absorption, probability of finding a photon at depth x in the material is given as:

$$P = \text{e}^{-x/\lambda}, \tag{3.10}$$

where λ is *attenuation length* (or absorption length), which is the photon path length into a material when the probability that the photon has not been absorbed is dropped to $1/\text{e}$. The probability that a photon will be absorbed by the material is given by the sum of all dominant interaction probabilities, i.e., for

^{28}Si - the photoelectric effect, Compton scattering, and pair production. X-ray attenuation lengths for ^{28}Si and for ^{208}Pb are shown in Figure 3.4. The graphs show, that the attenuation length of X-rays in lead is much smaller for the same photon energy, which makes lead a good material for shielding against radiation.
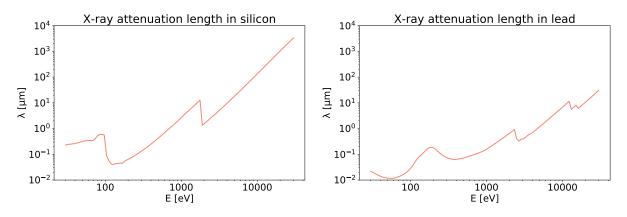

Figure 3.4: Photon attenuation length in ^{28}Si (left) and ^{208}Pb (right). Data taken from [90].

How deep into material an electron or a heavy particle will penetrate is given by the stopping power $S(E)$, which is the average linear rate of particle energy loss:

$$S(E) = -\left\langle \frac{\mathrm{d}E}{\mathrm{d}x} \right\rangle. \tag{3.11}$$

The precise equation of the stopping power was derived by Hans Bethe in 1930-1932 [91]. In literature, the mass stopping power is often used, which is the stopping power divided by density of the material and is given in units MeV cm^2 g^{-1}.

From the stopping power one can derive particle range in a material until it is absorbed. Particle distance in a material is usually calculated as continuous slowing down approximation range (or the CSDA range) as in [92] (with an approximation in $S(E)$):

$$R(E_0) = \int_0^{E_0} \frac{\mathrm{d}E}{S(E)}, \tag{3.12}$$

where E_0 is the particle initial energy, and $S(E)$ is the stopping power of the material (3.11).

In terms of this thesis, the most important is the range of electrons in ^{28}Si, which are the Compton electrons from the surrounding material, i.e., lead shielding. The electron range in ^{28}Si is shown in Figure 3.5. However, the electron trajectory in a material would not be a straight line and will be affected by the interaction of the electron with the material. While SXR photons become absorbed during interactions with silicon, electrons with energies up to 1 MeV can travel distance over 1 mm while spending their energy. In pixel detector, depending on the scattering angle, energetic electrons can interact in more than one pixel.
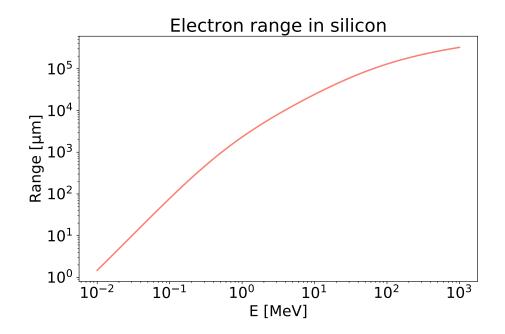
Figure 3.5: Electron continuous slowing down approximation range in ^{28}Si. Data taken from [93].

Chapter 4

Semiconductor detectors

4.1 Semiconductor materials

All materials, depending on their ability to conduct electric current, can be divided into three groups: insulators, which do not conduct electric current, conductors, through which electric current may pass freely, and semiconductors, whose conductivity lies between insulators and conductors. Generally, properties of these materials, including electrical conductivity, are dictated by the crystal lattice structure and electronic structures of atoms. It is well known that electrons, depending on their energy, can occupy different atomic orbitals, to which correspond different energy levels. In terms of electrical conductivity, the whole population of electrons in a material is separated between two groups. Electrons bound in the outer atomic shells form a so-called *valence band*. Electrons that leave the atomic shell and freely migrate through the material form a so-called *conduction band*. More electrons in the conduction band mean better electrical conductivity. The probability that the atomic orbital with the corresponding energy E is occupied is given by the Fermi-Dirac distribution (assuming a thermodynamic equilibrium):

$$f(E) = \frac{1}{1 + \exp(\frac{E - E_F}{k_B T})}, \tag{4.1}$$

where E_F is the so-called *Fermi level*, which corresponds to the level with probability of $\frac{1}{2}$ being occupied, and T is the absolute temperature. In semiconductors, the Fermi level lies between the conduction and valence bands and its position depends on the type of the semiconductor.

Conduction and valence bands are divided by a *band gap*, which is a region where electrons are forbidden. The distance between the bands is defined as the band gap energy E_g. The relative position of the both bands for an insulator, a conductor, and a semiconductor is schematically shown in Figure 4.1. Insulators, by definition, are not good electric conductors because of the large band gap energy $E_g > 5$ eV. On the other hand, conducting materials have many free electrons due to the overlapping conduction and valence bands. In semiconductors, band gap energy is close to unity [94].

Generally, band gap energy is the energy required for an electron to leave the valence band and become free contributing to the electrical conductivity. In reality, however, the situation is more complicated due to different quantum numbers of electrons in the atomic shell. A better representation of the valence and conduction bands in three different semiconductors is shown in Figure 4.2.

Figure 4.2 gives an example of semiconductors with a direct band gap (GaAs) and indirect band gaps (Ge, Si). Generally, Bloch's theorem states, that energy eigenstates (or stationary states) of electrons in the atomic shells of solids can be described by the Bloch waves:

$$\psi(\mathbf{r}) = e^{i\mathbf{k}\cdot\mathbf{r}} u(\mathbf{r}), \tag{4.2}$$
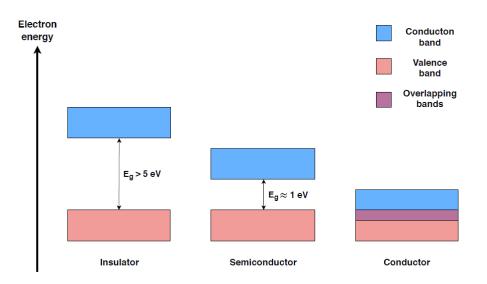
Figure 4.1: The conduction and the valence bands for an insulator, a conductor, and a semiconductor with approximate band gap energies. For a conductor, both bands overlap bringing free electrons to the conduction band and giving the material high electrical conductivity.

where $\mathbf{r}$ is the position vector, $\mathbf{k}$ is the crystal momentum vector, and u is a periodic function with the same periodicity as the crystal lattice. If the wave vector $\mathbf{k}$ is the same for the minimal state in the conduction band and for the maximum state in the valence band, then the band gap is direct. In other cases, the band gap is indirect. The statement, that the band gap energy equals energy required for an electron to get to the conduction band from the valence band, is valid only for the materials with a direct band gap. In this case, a single photon with sufficient energy $h\nu \geq E_g$ is enough to free an electron from the valence band. However, as can be seen from Figure 4.2, in case of an indirect band gap, an electron moving between the bands has to change its momentum. In this case, electrons have to emit or absorb a phonon, which is a quasiparticle that describes thermal vibrations in the material crystal lattice. The band gap energy in, e.g., Si is $E_g \approx 1.11$ eV at $T = 300$ K [96], while the average energy of an incident particle or a photon required for an electron-hole pair generation is ≈ 3.65 eV [97]. Dependency of the band gap energy on the temperature is given by the Varshni equation [98]:

$$E_g(T) = E_g(0) - \frac{\alpha T^2}{(T + \beta)},\qquad(4.3)$$

where $E_g(0)$ is the band gap energy at $T = 0$ K, α and β are the fitting constants.

Generally, there is an empirical relation between the band gap energy and the energy threshold for a pair of charge carriers generation in a semiconductor [99]:

$$E_{\text{thr}} \approx 3E_g.\qquad(4.4)$$

Several attempts to derive an analytical explanation of this relation were taken with different approximations, i.e., the free particle approximation with energy and momentum conservation [100], [101] among others.

In terms of this work, understanding the actual structure of the valence and conduction bands is not necessary. However, it was important to mention that Figure 4.1 serves only as a representation. For more in-depth descriptions of the problem and solid-state physics in general see references [96], [102].
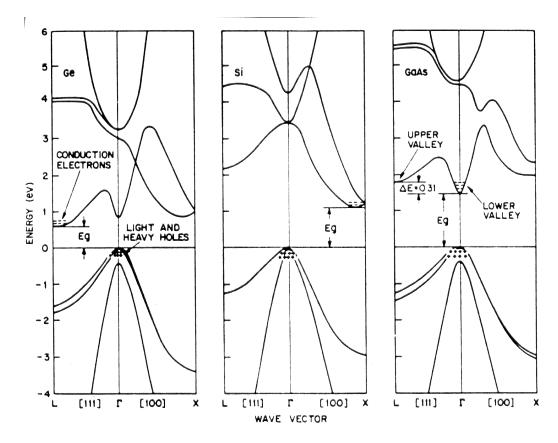
Figure 4.2: The valence (negative energies) and the conduction (positive energies) bands for Ge (a), Si (b) and GaAs (c) semiconductors. Ge and Si represent semiconductors with an indirect band gap, GaAs - with a direct band gap [95].

4.2 Charge carriers

At low temperatures all electrons stay bound to the atoms - in terms of a band diagram, electrons will be in the valence band. Higher temperatures bring more thermal vibrations into the crystal lattice of the material. If an electron will absorb enough energy, it will break its bonds with the atom and will get to the conduction band. In the valence band, the absence of an electron will create a hole with a positive charge. Such electron-hole pairs act as charge carriers in semiconductors.

In intrinsic, or pure, materials, number of electrons and holes is the same. The Fermi-Dirac distribution (4.1) can be obtained separately for both electrons and holes in an intrinsic semiconductor. Assuming $E - E_F \gg k_B T$ (or for energies $E > E_F + 3k_B T$ or $E < E_F - 3k_B T$ [103]) one can write [96]:

$$
\begin{aligned}
f_n(E) &\approx \exp\left(\frac{E_F - E}{k_B T}\right), \\
f_p(E) &\approx \exp\left(\frac{E - E_F}{k_B T}\right),
\end{aligned}
\tag{4.5}
$$

where f_n is the distribution for the electrons in the conduction band, and f_p - for the holes in the valence band. Number of states in the unit volume for a small interval of kinetic energies dE_{kin} can be written in

31

the following form [104] (derivation may be found in, e.g. [96]):

$$N(E_{\text{kin}})dE_{\text{kin}} = 4\pi \left(\frac{2m^*}{h^2}\right)^{\frac{3}{2}} E_{\text{kin}}^{\frac{1}{2}} dE_{\text{kin}}, \tag{4.6}$$

where m^* is the effective mass of a particle defined as $\frac{1}{m^*} = \frac{1}{\hbar^2}\frac{d^2E}{dk^2}$ [96], and h is the Planck constant. Density of the electrons in the conduction band n then can be found by integrating the product of the density of states (4.6) and the distribution function f_{n} (4.5) over the kinetic energies of electrons:

$$n = \int_0^{+\infty} 4\pi \left(\frac{2m_{\text{n}}^*}{h^2}\right) E_{\text{kin}}^{\frac{1}{2}} \exp\left(\frac{E_{\text{F}} - E_{\text{kin}}}{k_{\text{B}}T}\right) dE_{\text{kin}}, \tag{4.7}$$

where m_{n}^* is the effective mass of electrons in the conduction band. Full energy of free electrons consists of the energy threshold E_{C}, which is the energy required for electrons to get to the conduction band, and their kinetic energy. Therefore, kinetic energy of free electrons may be written as:

$$E_{\text{kin}} = E - E_{\text{C}}. \tag{4.8}$$

Substituting (4.8) into (4.7) one will get :

$$n = 2\left(\frac{2m_{\text{n}}^*\pi k_{\text{B}}T}{h^{\frac{1}{2}}}\right)^{\frac{3}{2}} \exp\left(\frac{E_{\text{F}} - E_{\text{C}}}{k_{\text{B}}T}\right) = N_{\text{C}} \exp\left(\frac{E_{\text{F}} - E_{\text{C}}}{k_{\text{B}}T}\right), \tag{4.9}$$

where N_{C} is density of states in the conduction band.

Similarly, the density of states in the valence band is:

$$p = 2\left(\frac{2m_{\text{p}}^*\pi k_{\text{B}}T}{h^{\frac{1}{2}}}\right)^{\frac{3}{2}} \exp\left(\frac{E_{\text{V}} - E_{\text{F}}}{k_{\text{B}}T}\right) = N_{\text{V}} \exp\left(\frac{E_{\text{V}} - E_{\text{F}}}{k_{\text{B}}T}\right), \tag{4.10}$$

where m_{p}^* is the effective mass of holes in the valence band, and N_{V} is density of states in the valence band [104].

In intrinsic semiconductors, $n = p$. Taking a ratio of equations (4.9) and (4.10) one will get an equation for Fermi level in intrinsic semiconductor E_{i}:

$$E_{\text{i}} = \frac{E_{\text{C}} + E_{\text{V}}}{2} + \frac{k_{\text{B}}T}{2} \ln\left(\frac{N_{\text{V}}}{N_{\text{C}}}\right). \tag{4.11}$$

However, completely pure semiconductor materials are absent in nature. Moreover, it is also possible to modulate these materials artificially, creating so-called *extrinsic semiconductors*, which are the materials with specific impurity atoms in the crystal lattice that modify the material characteristics. Extrinsic semiconductor will be discussed in more detail in Chapter 4.3.

There are three main mechanisms of an electron-hole pair generation. The first one has been already discussed at the beginning of the section - thermal excitation. Probability of generation of a pair depending on the temperature is given in [94]:

$$P(T) \approx T^{\frac{3}{2}} \exp\left(-\frac{E_{\text{g}}}{2k_{\text{B}}T}\right). \tag{4.12}$$

The other two rely on optical excitation and ionizing radiation, which makes semiconductors suitable for both photon and charged particle detection. Physical processes, on which generation of an electron-hole pair relies, are described in Chapter 3. Most energetic photons (X-rays, gamma) and charged particles (especially heavy particles, such as α) generate more than one electron-hole pair. The mechanism by

which radiation penetrate through the material is briefly discussed in Chapter 3.4. In semiconductors put into an electric field, electrons undergo acceleration along the field lines. Between the collisions, electrons may achieve energies sufficient for an electron-hole pair production. Thus, the number of charge carriers may undergo multiplication which is a phenomenon used in certain silicon detectors [104].

The generation mechanisms described above are valid only for ideal semiconductors. Either during the fabrication process or as a result of radiation damage, different lattice defects may appear in the material structure. These defects will bring new energy states to the semiconductor, which can also appear in the band gap. The most undesirable for detectors are states close to the middle of the band gap, as they are an effective source of thermal electron-hole pairs [104].

4.2.1 Charge carriers movement

In the absence of electric and magnetic fields, both electrons and holes in a homogeneous semiconductor undergo chaotic motion as they move freely across the crystal lattice with an average kinetic energy $\frac{3}{2}k_{\mathrm{B}}T$. Movement of the holes is represented by the movement of electrons in the valence band: electron within the band may occupy the vacancy leaving a hole behind. In the presence of electric field, particles start to drift - accelerate between the collisions in the direction controlled by the electric field. Particle momentum gain due to electric field is $\mathbf{p} = m^*\mathbf{v} = Q\mathbf{E}\tau$, where τ is the mean free time (time between collisions). Drift velocities of the charge carriers can be written in the next form [104]:

$$
\begin{aligned}
\mathbf{v}_{\mathrm{n}} &= -\frac{e\tau}{m_{\mathrm{n}}^*}\mathbf{E} = -\mu_{\mathrm{n}}\mathbf{E}, \\
\mathbf{v}_{\mathrm{p}} &= \frac{e\tau}{m_{\mathrm{p}}^*}\mathbf{E} = \mu_{\mathrm{p}}\mathbf{E},
\end{aligned}
\tag{4.13}
$$

where μ_{n} and μ_{p} are the electron and hole mobilities. In strong electric fields, charge carrier velocities become saturated due to collisions and the linear dependency on $\mathbf{E}$ is not valid.

Besides acceleration, particles undergo diffusion as well. An inhomogeneous distribution of the particles across the material is the source of new forces:

$$
\begin{aligned}
\mathbf{F}_{\mathrm{n}} &= -D_{\mathrm{n}}\nabla n, \\
\mathbf{F}_{\mathrm{p}} &= -D_{\mathrm{p}}\nabla p,
\end{aligned}
\tag{4.14}
$$

where $D_{\mathrm{n}} = \frac{kT}{Q}\mu_{\mathrm{n}}$ and $D_{\mathrm{p}} = \frac{kT}{Q}\mu_{\mathrm{p}}$ are the diffusion constants for electrons and holes respectively.

Effect of the drift in an electric field $\mathbf{j} = Q\rho\mathbf{v}$ (where ρ is the particle density) and diffusion due to the charge separation $\mathbf{j} = -QD\nabla\rho$ together define the electric current densities in a semiconductor material:

$$
\begin{aligned}
\mathbf{j}_{\mathrm{n}} &= en\mu_{\mathrm{n}}\mathbf{E} + eD_{\mathrm{n}}\nabla n, \\
\mathbf{j}_{\mathrm{p}} &= en\mu_{\mathrm{p}}\mathbf{E} - eD_{\mathrm{p}}\nabla p.
\end{aligned}
\tag{4.15}
$$

The resulting electric current density in a semiconductor is then a combination of the two for both types of charge carriers:

$$
\mathbf{j} = \mathbf{j}_{\mathrm{n}} + \mathbf{j}_{\mathrm{p}}.
\tag{4.16}
$$

In magnetic fields, Lorentz force will bend trajectory of the charge carriers. This will build up a voltage between two opposite sides of the material, balancing the effect of the magnetic field. This is

known as the *Hall effect*, which can be used to measure particle velocity, mobility, and concentration. In addition, Hall effect proves the existence of holes as charge carriers in semiconductors [104].

The opposite process of the electron-hole pair generation is recombination. Electrons from the conduction band may come back to the valence band bringing thermal equilibrium into the system. Other mechanisms of recombination require either an impurity presence, which may create an energy level within the band gap, or presence of a third particle, typically another electron in the conduction band. In the case of energy levels present in the band gap, the mechanism is called trap-assisted recombination, or *Shockley-Read-Hall* recombination [105]. In the case of three particle recombination (for example, two electrons and a hole), the mechanism is called Auger recombination. The released energy of the electron, which recombines with a hole from the valence band, is absorbed by another electron in the conduction band. For more detailed descriptions of different recombination processes see, e.g., [103], [104], [106].
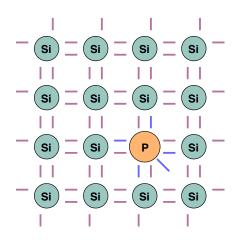
4.3 Extrinsic semiconductors

Intrinsic semiconductors are difficult to obtain because materials will always have some percentage of impurities. On the other hand, introducing certain impurities (often called "doping") may modify the material properties in a suitable way. Semiconductors with impurities are called *extrinsic semiconductors*. There are two ways to alter semiconductors: doping with elements with more or less valence electrons than the receiving material. Depending on which impurity is present in the crystal lattice, extrinsic semiconductors are divided into two groups: n-type and p-type semiconductors.

Semiconductors of the n-type are created via doping intrinsic material with impurities which have more valence electrons than the intrinsic material. For example, doping Si, which is tetravalent (4 valence electrons), with atoms of P, which is pentavalent, will bring one more electron per atom doped. When the atom of P replaces an atom of Si, 4 electrons of P will create covalent bonds with the neighboring atoms of Si. However, the fifth electron will stay without a pair and will be only loosely bound to the atom of P. Schematically this is shown in Figure 4.3. Elements with more valence electrons than the receiving material are called *donors*. The loosely bound electron at energy level E_D requires much less energy than the other electrons to become free and enter the conduction band. This affects the Fermi level, shifting it closer to the conduction band, as there is a higher probability that the electron will occupy a state in the conduction band. Band diagram of an n-type semiconductor is schematically shown in Figure 4.4. In case of Si, band gap energy is $E_g = E_C - E_V = 1.11$ eV, while $E_C - E_D = 0.045$ eV (for $T = 300$ K) [104]. Therefore, at a room temperature, all donor electrons will enter the conduction band. In n-type semiconductors, the balance between electrons in the conduction band and holes in the valence band is shifted, as there are more free electrons. This gives the name "n-type semiconductor", because there are more negative charge carriers.

Doping a semiconductor material with elements that have fewer valence electrons will create a semiconductor of the p-type. Doping Si with, for example, atoms of B, which is trivalent (3 valence electrons), will leave an electron of one of the neighboring Si atoms alone. This will create an electron vacancy in the crystal lattice (see Figure 4.5). Elements with fewer valence electrons than the receiving material are called *acceptors*. Acceptors introduce energy levels E_A into the band gap which are closer to the valence band, see Figure 4.6. For Si doped with B, the difference between the acceptor energy level and the valence band energy level is $E_A - E_V = 0.045$ eV [104]. Therefore, these states will be filled with electrons from the valence band. The balance between the charge carriers is shifted because there are more holes in the valence band than free electrons in the conduction band. This gives the name "p-type semiconductor", as there are more positive charge carriers.

Both donor E_D and acceptor E_A energy levels affect the Fermi level, which will be different from the one of intrinsic semiconductor (4.11). In case of complete ionization of donor impurities, it is safe to say
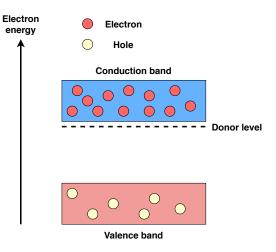
Figure 4.3: Crystalline lattice structure in silicon doped with phosphorus - example of n-type semiconductor. Each dash represents an electron, the impurity atom has one electron that is loosely bound.
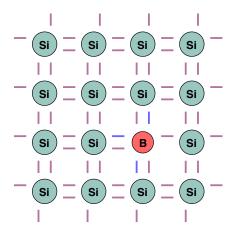

Figure 4.4: Energy band structure in the n-type semiconductors. Electrons in the conduction band are the majority carriers. Donor level represents lower energy level for impurities' electron.
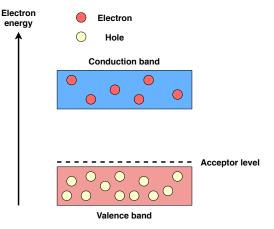

Figure 4.5: Crystalline lattice structure in silicon doped with boron. Each dash represents an electron, the impurity atom has a vacancy representing a hole.

Figure 4.6: Energy band structure in the p-type semiconductors. Holes in the valence band are the majority carriers. Acceptor level represents higher energy level for impurities' holes.

that the electron density in the conduction band is given by the donor concentration $n = N_D$. Combining this with the equation for electron density (4.9) one will get:

$$E_C - E_F = k_B T \ln\left(\frac{N_C}{N_D}\right). \tag{4.17}$$

Similarly, in case of complete ionization of acceptor impurities, $p = N_A$ with (4.10) gives:

$$E_F - E_V = k_B T \ln\left(\frac{N_V}{N_A}\right). \tag{4.18}$$

Higher the acceptor or donor impurity concentration in the material, the closer is Fermi level to the corresponding band. For an extrinsic semiconductor, it is possible to write equations (4.9) and (4.10) in terms of the intrinsic Fermi level and charge carriers density:

$$
\begin{aligned}
n &= n_i \exp\left(\frac{E_F - E_i}{k_B T}\right), \\
p &= n_i \exp\left(\frac{E_i - E_F}{k_B T}\right).
\end{aligned}
\tag{4.19}
$$

Since there are more electrons in the n-type semiconductors and more holes in the p-type, these charge carriers are called *majority carriers*. Holes in the n-type and electrons in the p-type semiconductors are called *minority carriers*.

4.4 The p-n junction, metal-semiconductor contact, and a metal-insulator-semiconductor structure

4.4.1 The p-n junction

A combination of the semiconductors of different types will create structures with distinctive characteristics. The most frequently used is the p-n junction, which are the p-type and n-type semiconductors put together. Usually, p-n junctions are produced via varying doping of the two opposing sides of a complete semiconductor crystal. Due to the different amounts of free electrons and holes in both sides, the particles will undergo diffusion: electrons from the n-type side will be pushed to the p-type and vice versa in case of the holes. In the p-type, electrons recombine with the holes creating a negative space charge. In the n-type side, a positive space charge will form. This charge separation leads to a generation of an electric field over the junction. This can be calculated using the Poisson equation:

$$
\nabla^2 \phi = -\frac{\rho}{\varepsilon},
\tag{4.20}
$$

where ϕ is the electric potential, and ε is the absolute permittivity of the material. Electric field is then given as:

$$
\mathbf{E} = -\nabla\phi.
\tag{4.21}
$$

The region where both types of semiconductors come to contact and where charge separation occurs is called the *depletion region*. Width of the depletion region is given by [104]:

$$
d = \sqrt{\frac{2\varepsilon(N_A + N_D)}{Q N_A N_D} V},
\tag{4.22}
$$

where V is the potential across the junction. The electric field in that region compensates the charge diffusion inducing a drift motion for both electrons and holes. The resulting current is then given as (4.15). Any electrons that occur in the depletion region are swept by the electric field into the n-type side of the junction, and holes - into the p-type. The potential difference across the depletion region is called *contact potential* V_{cp}. In thermal equilibrium, the contact potential is almost as large as the band gap energy. Schematically, p-n junction is shown in Figure 4.7. The contact potential is given by [104]:

$$
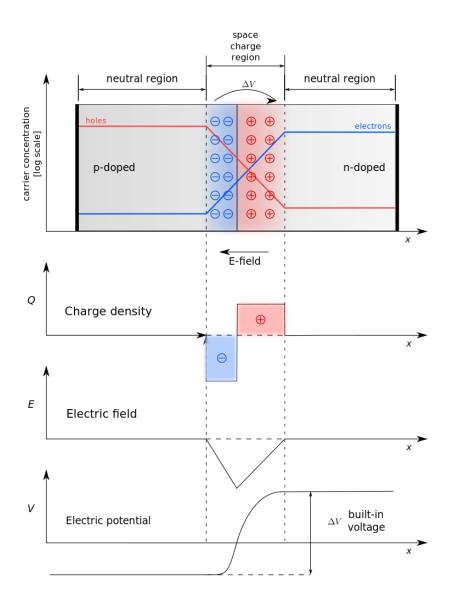V_{cp} = \frac{k_B T}{Q} \ln \frac{N_A N_D}{n_i^2},
\tag{4.23}
$$

Figure 4.7: A semiconductor p-n junction with zero bias voltage. Charge separation create a depletion region close to a contact of the two extrinsic semiconductor types which leads to a generation of electric field and a buildup voltage [107].

where $n_i^2 = np$.

A p-n junction with an external voltage applied through the electrodes on both sides of the junction (anode on the p-type side and cathode on the n-type side) will create a semiconductor diode. The voltage can be applied in two ways. The first one is to apply a positive voltage to the anode. This will attract electrons from the n-type and holes from the p-type side of the junction. In this case, these are the majority carriers, which will lead to an increased conductivity across the junction. This is called *forward biasing* and it is frequently used for an electric current rectification. If, however, a negative voltage will be applied to the anode, then it will attract holes from the n-type and electrons from the p-type side, which are the minority carriers. This will lead to a decreased conductivity. This is called *reverse biasing*.

37

The resulting voltage across the junction will be:

$$V = V_{cp} - V_{ext}, \tag{4.24}$$

where V_{ext} is the applied voltage. Substituting (4.24) into (4.22) one will get width of the depletion region with an external voltage applied. In case of a negative voltage applied, the depletion region width will be larger than in case of a positive voltage.

P-n junctions are the basic semiconductor structures that are utilized in electronics (e.g., p-n-p bipolar transistors) or radiation sensors and particle detectors. More on the p-n junctions can be found in, e.g., [94], [103], [104], [108].

4.4.2   Metal-semiconductor contact

A metal-semiconductor contact was the first practical semiconductor device used in electronics with first applications dating 1904 [103] (the p-n junction was discovered in 1940 by American electrochemist Russel Ohl [109]). A schematic of the contact is shown in Figure 4.8. The key characteristic is the work function $Q\phi$ which is the average energy required for an electron to leave the material. It is defined as the difference between the vacuum level (energy of a free stationary electron outside the material) and the Fermi level. Metals are known for their good electrical conductivity due to the abundance of free electrons in the conduction band. Because of that, the Fermi level in metals lies in the conduction band. The work function depends on the material properties or doping concentrations in case of semiconductors. Depending on the two materials used in a metal-semiconductor contact, the structure may behave either like a diode, also known as Schottky barrier, or an ohmic contact. Consider a metal-semiconductor contact with the metal work function higher than the one of a n-type semiconductor: $Q\phi_m > Q\phi_s$. When both materials are in contact, Fermi levels will become lined up in thermal equilibrium. Because of that, a built-in potential V_{bi} will form, pushing electrons from the conduction band of the semiconductor into the conduction band of the metal. However, these electrons well see a barrier of height $Q\phi_b = Q\phi_m - Q\chi$, where $Q\chi$ is the width of the conduction band in the semiconductor, see Figure 4.9. In case of a p-type semiconductor, the barrier height will be: $Q\phi_b = E_g - (Q\phi_m - Q\chi)$. For large barrier heights, the metal-semiconductor contact will form a Schottky diode. In the case of small barrier heights, the electrons from the semiconductor conduction band will also tunnel through the barrier, lowering the resistance and creating an ohmic contact as a result [103], [104]. In electronics, Schottky diodes are fast but suffer from large reverse currents. In semiconductor detectors, especially on a high-resistivity silicon, a Schottky contact is an unwanted feature on the backside of the sensor. This is usually mitigated by a strong shallow doping with the same polarity as the bulk material of the sensor. Then the metal layer for contacting is deposited.
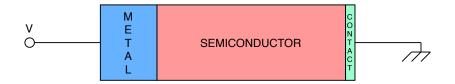

Figure 4.8: A metal-semiconductor contact. The metal is shown in blue, the semiconductor in red, and an ohmic contact in green. Voltage can be applied to the metal, the opposite ohmic contact is grounded.
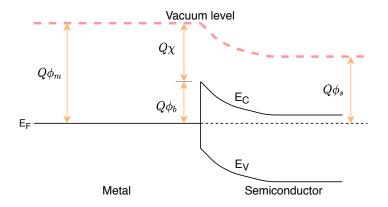
Figure 4.9: A band diagram for a metal-semiconductor contact. Depending on the barrier height $Q\phi_b$ the structure will from either a Schottky diode or an ohmic contact.

4.4.3 Metal-insulator-semiconductor structure

The metal-insulator-semiconductor structures (often called metal-oxide-semiconductor, or MOS, because, i.e., for Si, the insulator is usually SiO_2) play crucial role in modern electronics. A MOS capacitor combined with two p-n junctions will create a so-called MOSFET (Metal-Oxide-Semiconductor Field-Effect Transistor), which is the key part of microprocessors. In terms of detectors, pixel and strip hybrid detectors - or, precisely, the detector sensors - are produced in CMOS (Complementary Metal-Oxide-semiconductor) technology when a MOS capacitor is combined with p-n diodes. The composition of a MOS capacitor is schematically shown in Figure 4.10: for a silicon p-type substrate, the metal can be, i.e., aluminum, the insulator - SiO_2, and the backside of the silicon can be covered also in aluminum, providing an electric contact for, in the case of detectors, biasing. The band diagram for such MOS structures with $V = 0$ bias voltage is shown in Figure 4.11: similar to the case of the Schottky barriers (see Figure 4.9) $Q\phi_m$ is the metal work function, $Q\phi_s$ is the semiconductor work function, $Q\phi_b$ is the barrier height, and $Q\chi$ is the electron affinity, or difference between the semiconductor conduction band edge and the vacuum level.
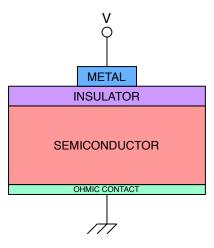

Figure 4.10: A schematic of a MOS capacitor. The metal is shown in blue, the semiconductor in red, and the insulator is shown in purple. Voltage can be applied to the metal, the opposite ohmic contact (in green) is grounded.
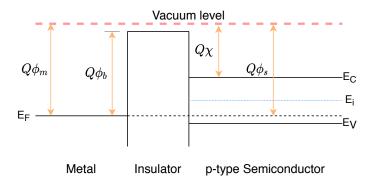
Figure 4.11: A band diagram for a MOS capacitor with a p-type semiconductor and no bias voltage applied. The insulator that divides the metal and the semiconductor will create a barrier of height $Q\phi_b$, similarly to the Schottky diode.

Assume an ideal MOS capacitor, which means there is no other charge carriers under any biasing voltage than the charges in the semiconductor and the metal with no charge carrier transport through the insulator. In that case, the Fermi level E_F in the semiconductor will remain constant under any biasing. However, there can be three distinct situations in a MOS capacitor, depending on the biasing voltage applied.

For a negative biasing voltage $V < 0$ applied to the metal (often called the *gate*), the positive charge carriers in the semiconductor - holes - will become attracted to the metal (see Figure 4.12). This will lead to an accumulation of holes on the insulator-semiconductor edge and, therefore, bending the semiconductor energy bands slightly upwards (including the intrinsic semiconductor Fermi level E_i, see (4.11)). Hence, a built-in voltage across the insulator will appear. This is called *accumulation case*.
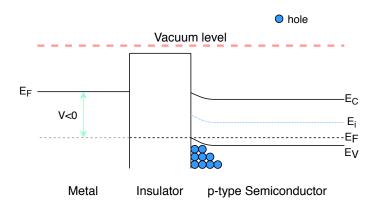

Figure 4.12: A band diagram for a MOS capacitor with a p-type semiconductor and a $V < 0$ bias voltage applied - the accumulation case. The semiconductor energy bands are bent upwards. The holes (in the valence band) are attracted to the negative voltage and are accumulated at the insulator-semiconductor edge.

For a positive biasing $V > 0$ applied to the gate, holes in the semiconductor will be repelled bending the energy bands slightly downwards (see Figure 4.13). Therefore, the region in the semiconductor near the insulator edge will become depleted - this is called the *depletion case*.

For a larger positive voltage applied to the gate, the semiconductor bands will bend downwards even more. Opposite to the accumulation case, electrons from the semiconductor will become attracted to the insulator edge (see Figure 4.14). This is called the *inversion case*. MOS capacitors at such overdepleted
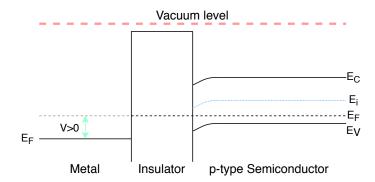
Figure 4.13: A band diagram for a MOS capacitor with a p-type semiconductor ans a *V* > 0 bias voltage applied - the depletion case. The semiconductor energy bands are bent downwards. The holes are repelled by the positive voltage leaving depleted region near the insulator-semiconductor edge.

states can serve as a detector. Charge carriers (electrons in the case of a p-type substrate and holes in the case of an n-type substrate) generated by the ionizing radiation in the depleted region in the semiconductor will move to the semiconductor-insulator edge inducing charges on the metal electrode. Further, this induced charge can be measured. Charge carriers near the semiconductor-insulator edge can be also collected with electrodes [104].
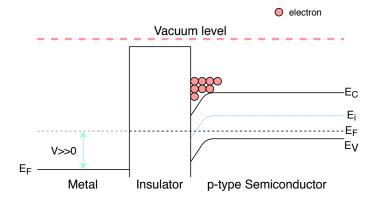

Figure 4.14: A band diagram for a MOS capacitor with a p-type semiconductor ans a *V* >> 0 bias voltage applied - the inversion case. The semiconductor energy bands are strongly bent downwards. The semiconductor free electrons (in the conduction band) are attracted to the strong positive voltage and are accumulated near the insulator-semiconductor edge.

Similar assumptions but with some distinctions are valid for a MOS capacitor with a n-type substrate. For a detailed description see, e.g., [104].

4.5 Semiconductor detectors

Intrinsic unbiased semiconductor detectors can be used as radiation level detectors. In this case, an electric current induced by the radiation directly is measured. However, extrinsic semiconductors are more suitable for a semiconductor detector. An ordinary p-n junction with no external voltage applied (but with electrodes to collect charges) may serve as a detector. Both photons and charged particles flying across the depletion region will generate electron-hole pairs, which due to the buildup potential will be

swept away in the opposite directions towards electrodes. However, the contact potential in this case is relatively small, and charge carriers will not gain sufficient energy to survive and reach the electrodes as they will recombine. Therefore, to make an effective detector, an external voltage should be applied. Reverse biasing is preferable as it widens the depletion region and lowers the current noise across the junction. There are limits on the voltage applied, as for high values, a breakdown may occur: a sudden increase of the current across the junction which may damage the detector electronics. Usually, fully depleted junctions are used for detection purposes as they enhance the effectivity of the detector.

When ionizing radiation enters the sensor, its energy is spent on ionization of the surrounding atoms through collisions with electrons in the case of charged particles, the photoelectric effect or Compton scattering of photons interacting with electrons, and the pair production mechanism in the case of highly energetic photons interacting with nuclei. The number of electrons (or holes, as they are equal) M generated is given as:

$$M = \frac{E}{\epsilon}, \tag{4.25}$$

where E is the energy of the ionizing radiation absorbed by the sensor, and ϵ is the mean energy required for a generation of an electron-hole pair (3.65 eV for Si at $T = 300$ K). The difference between E and the energy spent on the charge carriers generation is emitted in phonons. However, the average number of pairs generated is not always exact and constant as it is affected by different fluctuations. Therefore, the variance in the number of electrons (or holes) generated is given as [110]:

$$\langle \Delta M^2 \rangle = F \cdot M = F \frac{E}{\epsilon}, \tag{4.26}$$

where F is the Fano factor. The measured values of the Fano factor for Si are $\approx$ 0.1 [110], [104]. For example, scintillation detectors have the Fano factor values close to unity. Assume a detector that measures an energy distribution of the incident radiation from a monoenergetic source. The energy resolution defined as $R = \frac{FWHM}{H_0}$, where $FWHM$ is the full width at half maximum of the signal, and H_0 is the average pulse height, can be written in terms of the Fano factor as follows [94]:

$$R = 2.35 \sqrt{\frac{F}{M}}. \tag{4.27}$$

A small Fano factor F of the semiconductor materials combined with the low energy required for a generation of an electron-hole pair (large M compared to the other detectors, e.g., scintillation detectors) defines good energy resolution of the semiconductor detectors.

The collection of the charge carriers is conducted on electrodes. However, according to the Shockley-Ramo theorem, an electric current on the electrodes will be induced due to the moving charge carriers [111], [112]. Therefore, to generate a signal, the particles do not have to reach the electrode. The induced current is given as:

$$I = \frac{QE_{\mathrm{v}}v}{V}, \tag{4.28}$$

where E_{v} is the component of the electric field in the direction of the particle velocity v and V is the biasing potential applied to the electrode. For a more detailed review of the Shockley-Ramo theorem see, e.g., [113]. Via a charge-sensitive amplifier (CSA) [114] the signal is transformed into an output voltage, which can be afterwards processed in a desirable way. Realization of a CSA in an electric circuit is shown in Figure 4.15. The output voltage is given as [104]:

$$V_{\mathrm{out}} = -\frac{Q_{\mathrm{in}}}{C_{\mathrm{f}} + \frac{C_{\mathrm{D}} + C_{\mathrm{in}} + C_{\mathrm{f}}}{A}}, \tag{4.29}$$
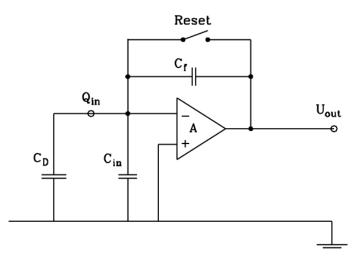
Figure 4.15: Charge-sensitive amplifier for signal collection in semiconductor detectors. The input charge is collected and transformed into the output voltage. The switch (reset) is necessary to discharge the C_f capacitor and keep the signal from stacking up [104].

where Q_{in} is the charge collected, C_f, C_D, C_{in} is the detector, feedback, and input capacitance respectively, and A is the coefficient of the voltage amplification $V_{out} = AV_{in}$.

However, in all semiconductor junctions there are leakage currents present due to the nature of a junction (for example, a minority carriers diffusion in a reverse bias configuration) and thermal generation of electron-hole pairs (other sources of noise in detectors are discussed in, e.g., [104]). Such currents, that are not induced by the incoming radiation or particles, act as a noise in the resulting signal. In Si at room temperature, however, there almost no thermal noise due to the indirect band gap (Ge detectors have to operate with cryogenic cooling due to the high thermal noise at room temperatures). To distinguish the actual detected signal from the noise in the detector, there is a certain voltage threshold which is set externally (for example, via a PC) and which separates the actual signal from the noise. Measuring time (or precisely, a pulse width of the digital output) for which the measured signal spent over the threshold provides information about the energy of the incoming radiation. This method is called Time-over-Threshold (ToT) [115].

Besides the diode itself, another important part of the detector is the electronics that conducts the primary processing of the signal (shaping, amplification) and provides a connection between the detector and a PC. The signal readout can be both analog and digital. In the analog readout, the signal amplitude is measured. The transformation to the digital signal is conducted in a Analog-to-Digital Converter (ADC). If a noise control is applied via voltage threshold settings, a Digital-to-Analog Converter (DAC) is also present in the electronics. The electronics and the silicon sensor of the detector can be manufactured either separately and then put together via conductive connections (this is often called "flip-chip" configuration of the hybrid semiconductor detectors, see Figure 4.16) or both can be manufactured on a single piece of material (monolithic detector).

Reverse biasing of the semiconductor diodes is often used for energy measurements of radiation. However, if these diodes will be put side by side in a strip (parallel lines of diodes) or a pixel (matrix) composition, the resulting setup will make possible position measurements, where the position is given by the strip or pixel where the signal was generated. An example of a strip detector is shown in Figure 4.17 and an example of a pixel detector is shown in Figure 4.18 with a schematic of a pixel structure shown in Figure 4.19. In both setups, each diode is connected to an ASIC (Application Specific Inte-
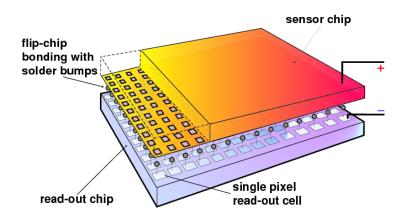
Figure 4.16: An example of a flip-chip configuration of a hybrid semiconductor pixel detector. Each pixel consists of a sensor - active volume where ionizing radiation interacts with the material and generates charge carriers - with readout electronics which are connected via a conductive bump. The external part of the sensor is covered in a metal creating an ohmic contact for biasing (not shown) [116].

grated Circuit) which conducts the primary processing of the signal output. Data transfer between the detector electronics and a controlling PC is provided by a specific readout system (for example, SPIDR [117]). The control of the whole setup is directed via software from a PC which allows to set the threshold level, acquisition window size, and conduct pixels calibration.

Figure 4.17: Strip detector PH32: Si sensor (brown) wire-bonded to the readout ASIC PH32 [118].
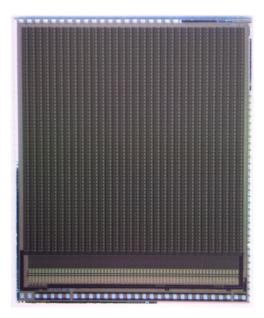

Figure 4.18: Monolithic pixel detector X-chip-03 used in earlier experiments [63], [119].
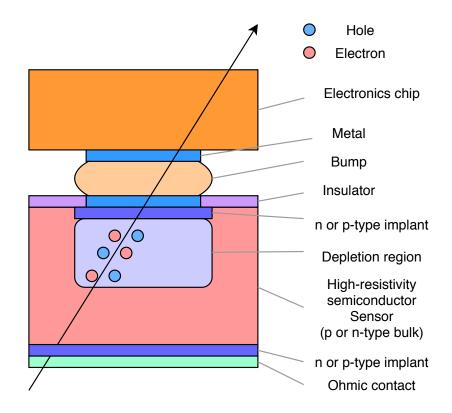
Figure 4.19: A schematic of a pixel structure of a hybrid pixel detector: the sensor and the readout electronics are connected by the flip-chip method via bumps. While the bulk semiconductor material can be either p or n-type, the implant is made of the opposite type semiconductor in order to prevent Schottky contacts. Depletion region is created via appropriate biasing and for detection purposes it spans across the whole semiconductor body. Ionizing radiation (photons will be absorbed while particles can penetrate through the whole pixel) upon entering the depletion region generates electron-hole pairs. The charge carriers are then collected via metal electrodes and analyzed by the electronics. Typical dimensions of the pixel are tens of μm.

Semiconductor detectors have certain advantages over other detectors. One of them is the low ionization energy: as was mentioned in Chapter 4.1, the average energy that the incident photon has to have in order to generate an electron-hole pair is $\approx$ 3.65 eV for T = 300 K. In comparison, gas-filled detectors have ionization energy about 30 eV and 100 eV is a typical value for the scintillation detectors [94]. Also, semiconductor detectors can be produced in compact dimensions, which can be required for measurements on spacecrafts. Moreover, these detectors have a high temporal and spatial resolution, as well as good radiation tolerance [104].

4.6 Timepix3

Timepix3 is the third generation in a series of pixel readout chips [120]. The chip was developed by the Medipix3 collaboration at CERN in a 130 nm CMOS technology. The key abilities of the chip is a recording of the time of arrival of the particle (or ToA) simultaneously with ToT. Another characteristic of the chip is a sparse readout (or data-driven readout), which means that pixels are actively readout only when a particle is detected. This makes possible faster readout of the whole pixel matrix. The chip

has a matrix of 256×256 pixels with a pixel size of 55×55 μm^2. The main purpose of the chip is a particle or radiation tracking. Nonetheless, photon counting is also possible for imaging applications. The chipboard is shown in Figure 4.20. The hybrid silicon detector with the Timepix3 chip (referred as "Timepix3 detector" further in the text) that was tested on a tokamak, which is discussed in Chapter 5, used a 200 μm thick Si p-type sensor which provided sensitivity to all charged particles and high detection efficiency for photons in the energy range from 3 to 15 keV. The sensor on the chipboard is shown in Figure 4.21.

Readout of the chip is directed by the general purpose readout system SPIDR developed at Nikhef [121]. The electronics of the readout system and the software that control the system operation are hosted by a PCB (Printed Circuit Board) with an FPGA (Field-Programmable Gate Array). Connection to the Timepix3 is conducted via a 10 GbE link. The system can handle up to 80 Mhits/s of data from the chip.

Figure 4.20: Timepix3 chipboard. The chip is covered with aluminium foil (to ensure an electric contact for biasing) with a hole that was cut off for experiments with lasers at Nikhef. The black plastic around the chip serves as a screen against stray light, the yellow kapton tape is to keep the chip clean and to ensure good transmission of X-ray photons.

Figure 4.21: The Timepix3 Si detection region. The sensor consists of 256×256 pixels with a pixel size of 55×55 μm^2 and it is bump-bonded onto the Timepix3 readout ASIC below [122].

Chapter 5

Experiments

5.1 COMPASS tokamak

The COMPASS tokamak has been the main focus of the thermonuclear fusion experiments at the Institute of Plasma Physics of Czech Academy of Sciences (IPP CAS) since 2006. It was originally operated by UKAEA (UK Atomic Energy Authority) at Culham under name COMPASS-D (COMPact ASSembly with a D-shape cross section of the vacuum chamber) until 2002. In 2006, the tokamak was offered to IPP CAS [123]. In 2008, the COMPASS tokamak had its first plasma on Czech land. The key characteristic of the tokamak is the ITER-like plasma geometry, which makes the machine highly relevant for preparations of the ITER experiment along with other European tokamaks with a ITER-like plasma shape: JET, Culham Center for Fusion Energy [124], and ASDEX-U, IPP Garching [125]. Two main research topics at the COMPASS tokamak are the edge plasma physics and the wave-plasma interactions. Since 2014, it also has been making systematic contributions to the RE research [71]. The key parameters of the tokamak can be found in Tab. 5.1. The COMPASS tokamak installed in the experimental hall at the IPP CAS can be seen in Figure 5.1 and the view of the tokamak vacuum vessel interior is shown in Figure 5.2.

Major radius	0.56 m
Minor radius	0.23 m
Vacuum pressure	10^{-6} Pa
Plasma current	< 400 kA
Toroidal magnetic field	$0.9 - 2.1$ T
Pulse length	≈ 400 ms
NBI heating	2×0.4 MW

Table 5.1: The main parameters of the COMPASS tokamak [126].

The main set of diagnostics utilized during the RE campaigns at the COMPASS tokamak includes:

- Magnetic diagnostics, including 24 Mirnov coils, 16 Rogowski coils, 8 flux loops;

- A set of scintillation detectors: unshielded NaI(Tl) detector for HXR measurements sensitive to radiation of energy 50 keV − 1 MeV, ZnS(Ag) detector shielded by 10 cm thick lead blocks for measurements of HXR with energy above 500 keV and neutrons;

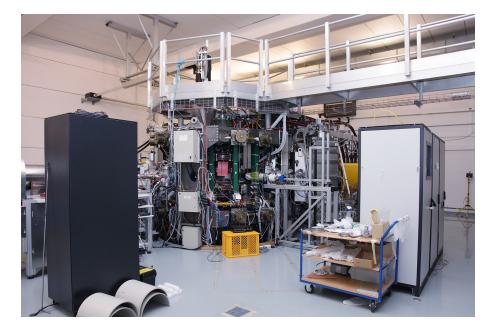- Thomson scattering for acquiring temperature and density profiles;

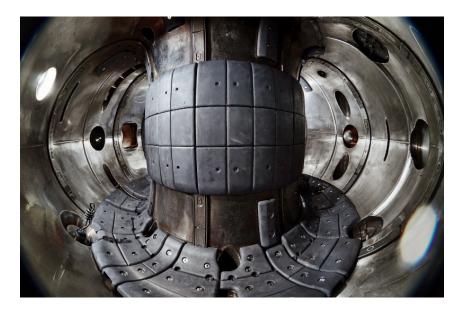Figure 5.1: The COMPASS tokamak in the experiment hall at the IPP CAS [126].

Figure 5.2: Interior of the COMPASS tokamak chamber. The tiles of the poloidal limiter made of graphite can be seen on the central column of the chamber. The bottom of the chamber is covered by the graphite divertor components [127].

- 6 pinhole cameras with 20 channel AXUV bolometers for SXR measurements providing spatial distribution of the plasma with a 1 μs temporal resolution;

- A set of fast cameras: two cameras Photron Mini UX100 and one Photron SA-X2;

- A calorimetric probe for the RE energy measurements;

- A Cherenkov detector.

The results presented in this thesis were acquired during the 11th RE campaign. The data were gathered by a Timepix3 detector during almost 150 plasma discharges. Besides the diagnostics mentioned above, an RTSP-injector (Room Temperature Solis-state Pellet) was also used during the campaign. Ar, Ne and Kr gasses were puffed during most of the shots to achieve disruption in order to study the REs generated during the event.

5.2 The experimental setup

The Timepix3 detector was installed at the radial midplane port with a clear view of the HFS, see Figure 5.3. The detector chipboard (Figure 4.20) was attached to a lead pinhole (Figure 5.4) and the whole structure was installed at the port with a Be window (Figure 5.5), which is used to ensure a good X-ray transparency. A PCB with an FPGA was attached to the chipboard via an FMC cable. 10 Gb Ethernet connection to the PC was provided by an optic cable. The detector sensor was biased to a -150 V by the high-voltage source-measure unit Keithley 237 that was connected via LEMO cable (Figure 5.6). The biasing current was measured to be in the order of 10 nA during the experiments.

As the RE intensity rose during the campaign, the Timepix3 detector started to be saturated. A saturation or a pile-up of the signals can arise due to two reasons: the frequency of events (ionizing radiation interactions with the sensor material) is higher than the readout electronics are capable of processing; the deposited energy is so large that the readout system cannot process it. The problem was solved via two methods: a set of 5 cm thick lead blocks was installed in front of the detector providing shielding against the incoming background radiation (the shielding was one block wide, see Figure 5.7) and number of the active pixels of the sensor was lowered in order to facilitate the sensor readout (Figure 5.8). The position of the smaller windows was selected due to the unusual results acquired during one of the shots which will be discussed later.

5.3 Results

In this section, only the most interesting and best results acquired with the Timepix3 detector are presented. More good results can be found in the Appendix.

The Timepix3 detector is able to collect different types of data: hits of the incoming ionizing radiation with the sensor together with the coordinates of the active pixels, which combined gives a map of the whole sensor - a "hitmap" (Figure 5.9), a ToA signal that shows the time distribution of arriving hits (Figure 5.10), a ToT signal (Figure 5.11), which with an energy calibration of the sensor can give an energy spectrum. The hitmaps presented in the text are composed in the following manner: the first row shows the actual window size of active pixels, the second row shows the window zoomed; the first plot in each row corresponds to the whole signal, the second - for the cluster size of 1 (mainly photons), the third - cluster size > 1 (particles, mostly Compton electrons from the shielding).

During each shot, a number of active pixels for each event is analyzed. For SXR photons, as they become absorbed during the interaction, only one pixel can be activated per event (rarely two because of
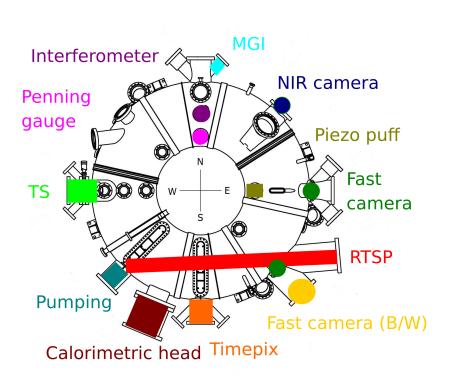
Figure 5.3: A schematic representation of the diagnostics utilized during the 11th RE campaign. The Timepix3 detector was installed at the south radial midplane port, shown in orange. The RTSP-injector is shown in red, set of three fast Photron cameras is shown in dark green (Photron Mini UX100) and yellow (Photron SA-X2). A Ne/Ar/Kr MGI is shown in light blue. Thomson scattering is shown in green. Courtesy of Jaroslav Čeřovský.
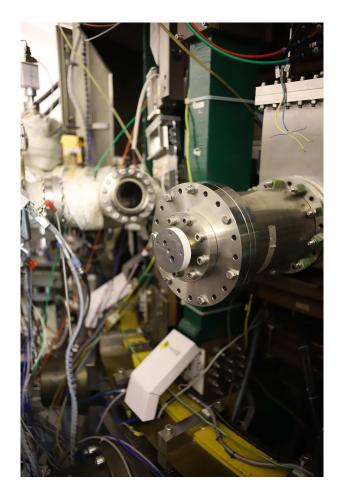
Figure 5.4: A lead pinhole attached to the south radial midplane port. The pinhole serves as a focusing lens for X-ray imaging.
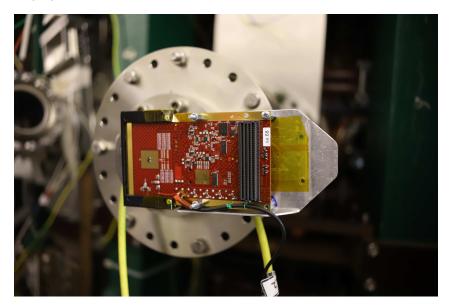
Figure 5.5: The Timepix3 chipboard attached to the lead pinhole. The cable at the bottom of the board is the biasing LEMO cable.
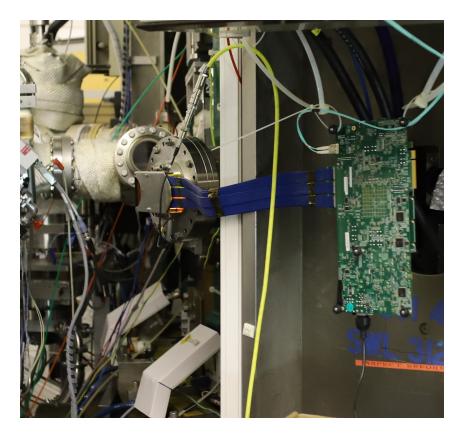
Figure 5.6: A complete setup of the detector. Due to the low flexibility of the FMC cable (the blue cable), the PCB board with an FPGA (green board in the middle) was hanged up besides the port on the support structure of the tokamak magnets. The yellow cable is the biasing LEMO cable; the light green cable is the 10 GbE optic cable.
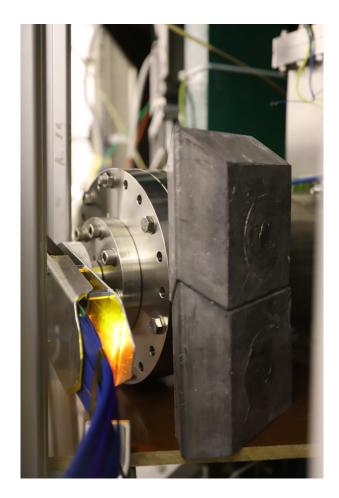
Figure 5.7: 5 cm thick lead blocks used as a shielding against gamma rays and Compton electrons for the Timepix3 sensor.
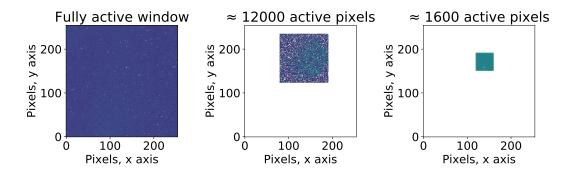
Figure 5.8: The Timepix3 ASIC has a matrix of 256×256 sensitive pixels. Different window sizes were used to overcome of the readout system saturation: fully active window (left), the pixels in the window with positions 80 - 190 × 123 - 233 are active (center), the pixels in the window 120 - 160 × 150 - 190 (right).
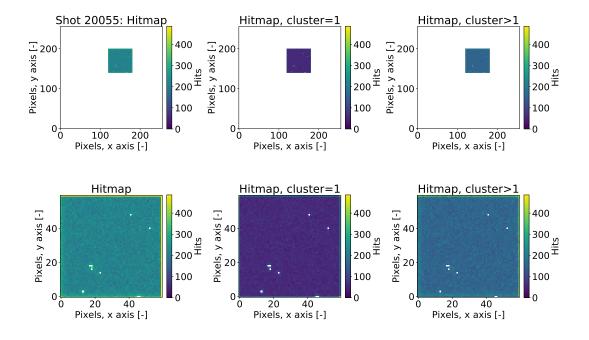
Figure 5.9: Shot 20055, the hitmap. The cause of bright edges lies in the hardware of the detector, the reason, however, is unknown. The white pixels are masked (not active) because they were noisy.
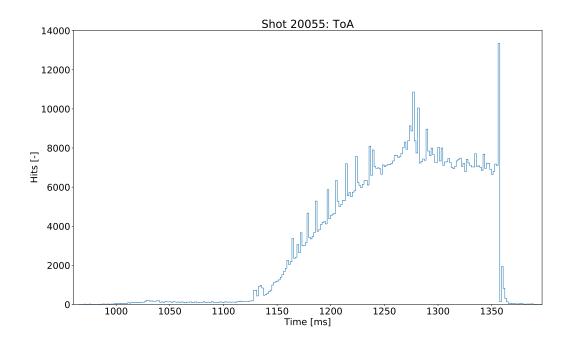
Figure 5.10: Shot 20055, ToA. The hits are plotted over time. With the trigger, the time axis corresponds with the diagnostics from the tokamak. The temporal resolution of the Timepix3 detector is 25 ns.

Figure 5.11: Shot 20055, ToT. The hits are plotted over ToT value. Combined with the energy calibration of the detector, it is possible to get an energy spectrum of SXR photons.
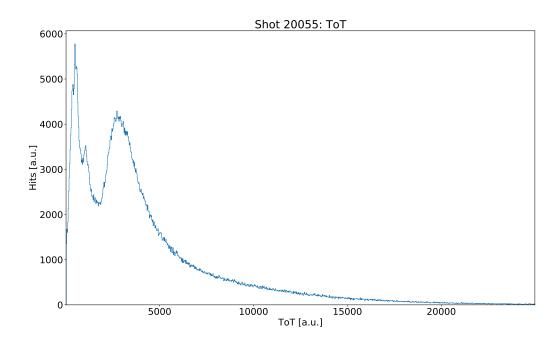
the so-called *cross-talk* of the neighboring pixels [110]). For particles, the number of active pixels per event is usually more than one, though that depends on the angle at which the particle hits the sensor. For the heavier particles, the number of pixels activated is higher. Therefore, it is possible to get a separation by the cluster size for each signal: see Figure 5.12 for the ToA, Figure 5.13 for the ToT (in Figure 5.9 the hitmap is divided for cluster size of 1 - photons - and > 1 - particles, mostly Compton electrons from the shielding). Combining the ToA and the ToT signal, one can get all three types of data (hits, the ToA, and the ToT) in one picture, see Figure 5.14.

A combination of different diagnostics that are crucial for the study of the RE physics - the plasma electric current (the Rogowski coil), HXR, SXR, neutrons (the shielded scintillation detector) - are plotted together with the ToA signal from the Timepix3, see Figure 5.15. It is important to mention, that due to the high RE intensity, the diodes for SXR measurement are presumably measuring HXR and the neutron signal may have some HXR background included. However, for conveniency, this signal will be referred as "SXR". In the figure, the Ar puff (used to achieve a disruption) is shown in orange. The number of active pixels is ≈ 1600 (see Figure 5.8), which allows the detector to operate without reaching a saturation. The shot ended with a disruption at 1357.05 ms, which can be seen in the loss of the plasma current and a peak in all RE diagnostics. The following peaks in the HXR and the ToA signals show, that some REs persevered for ≈ 6 ms after the disruption - a short-lived RE beam.

The reason for positioning the active window of the sensor was found in the shot 19977. It was a weak shot in terms of the REs generated, the scintillation detectors and the SXR detectors measured almost only noise. The ToA signal is shown in Figure 5.16. Nonetheless, it was a lucky shot for the Timepix3 as the low RE intensity lead to peculiar structures seen by the detector. The detector was operated with the full window active, see Figure 5.17. Due to the low RE intensity, the lead pinhole window was seen by the sensor. That area was later chosen as the active window for the shots with higher RE intensity in
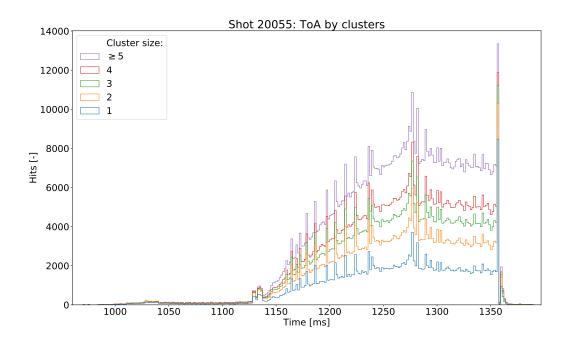
Figure 5.12: Shot 20055, ToA separated by cluster size. Cluster size of 1 corresponds to photons, > 1 to particles. The histograms are stacked one atop another.

hope of achieving more similar results.

During the last day of the campaign, a lot of previously unseen results were achieved with the Timepix3 detector. Due to the high RE intensity, the detector was operated with the smallest active window of ≈ 1600 pixels. At the initial stage of some shots, there were unusual structures seen by the detector. Figure 5.18 shows the hitmap from the shot 20068. The structure seen in the hitmap was obviously generated by highly intensive photons, as the pattern persevered for the whole event. In order to study the event, the time signal was cut into 100 intervals to find when the structures occurred. In Figure 5.19 and Figure 5.20, the first 15 out of 100 hitmaps are shown. While Figure 5.19 shows the hits collected in separate time intervals with length of each shown in the title of the corresponding image, Figure 5.20 shows the hits collected from the start of operation of the detector (the shot started at ≈ 950 ms) until the time shown in the titles of the images. The time intervals are not equal for a reason: as the detector is active only during the events (hits), it is impossible to divide the time signal into equal intervals with an equal time step. Nonetheless, it gives a perspective of how often the events happened. The two figures were generated for different reasons: while the collection of hits from the start of the shot in Figure 5.20 gives clear view of the structures seen, the separation into time intervals shows when the events occurred. The structures seen by the detector are thought to be the components of the tokamak limiter, as shown in Figure 5.2.

The limiter hit by the REs was also seen by the fast cameras: for example, a snapshot from one of the Photron Mini UX100 from the shot 20056 is shown in Figure 5.21 (in shot 20068, cameras had different settings for the pellet explosion study and the limiter is not seen; on the other hand, the signal measured by the Timepix3 detector in the shot 20056 is rather weak). The reason why these tiles radiate so much is because of REs that escape from the plasma hit the limiter. The tokamak diagnostics with the ToA signal from the Timepix3 are shown in Figure 5.22. As can be seen from the plot, the signal is rather
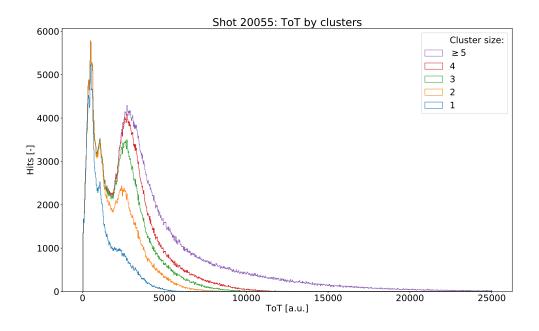
Figure 5.13: Shot 20055, ToT separated by cluster size. Cluster size of 1 corresponds to SXR photons, > 1 to particles. The histograms are stacked one atop another. While the photon signal is represented mostly by a single peak, the particles signal is represented by two peaks. The most energetic particles interact with more than 5 pixels.
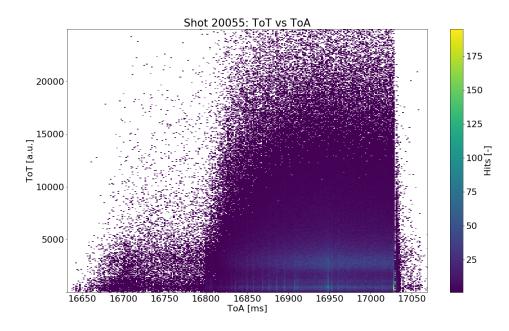
Figure 5.14: Shot 20055, a histogram of the ToT signal plotted over the ToA signal with number of hits of particular energy at particular time. The background (zero hits) is plotted in white.
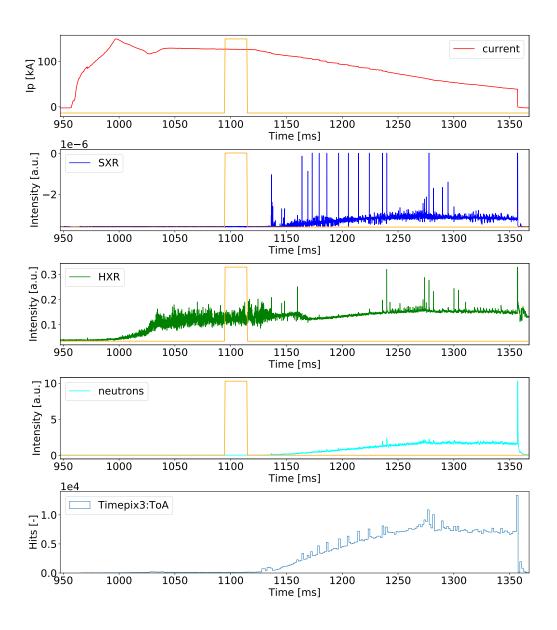
Figure 5.15: Shot 20055, the ToA signal from the Timepix3 plotted with the key RE diagnostics from the tokamak. The Ar puff is shown in orange. The shot ended with a disruption at 1357.05 ms.
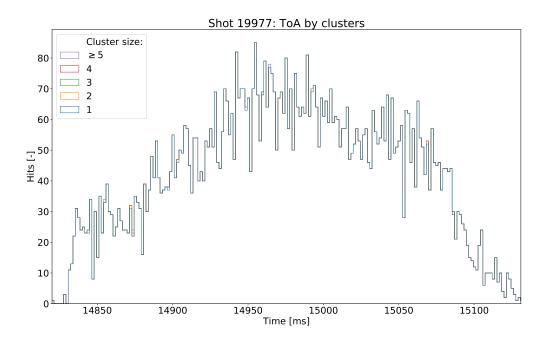
Figure 5.16: Shot 19977, ToA. The signal is dominated by the photons (the stacked histogram does not show any other parts that correspond to the larger clusters), however, of low intensity (not many hits compared to the other shots).
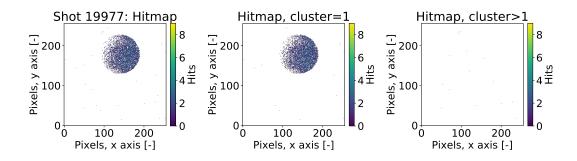
Figure 5.17: Shot 19977, the hitmap. The lead pinhole window is seen in X-rays by the detector as it was a shot with low RE intensity. That area was later chosen as the active window for the shots with higher RE intensity.
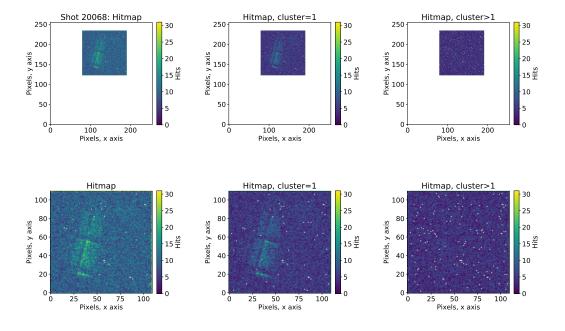
Figure 5.18: Shot 20068, the hitmap. The tokamak limiter on the HFS seen by the detector in X-rays.

weak at the time when the structures are well seen in the hitmap. Figure 5.20 also shows, that 15th out of 100 hitmaps generated corresponds to time 1093 ms, while the shot ended at $\approx$ 1162 ms. This is because of many events measured during the disruption. The disruption was initiated by a carbon pellet injected via the RTSP-injector. The pellet exploded in the plasma which was recorded by the fast cameras, see Figure 5.23 for a series of snapshots from the Photron SA-X2. In theory, the Timepix3 detector can be also used in the experiments with pellet injections providing an insight into the RE-pellet interactions. However, during the experiments at the COMPASS tokamak, the pellets (and their explosions) were out of the field of view of the Timepix3 detector.
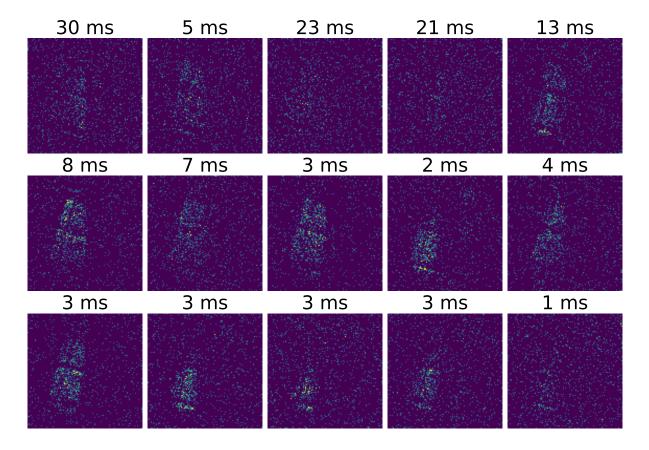
Figure 5.19: Shot 20068, first 15 out of 100 hitmaps generated from the separated time intervals. The intervals are separated in equal amount of frames with length of each interval shown in the title of the corresponding image. The narrowing of the time interval shows, that with the course of the shot the events happened more often.
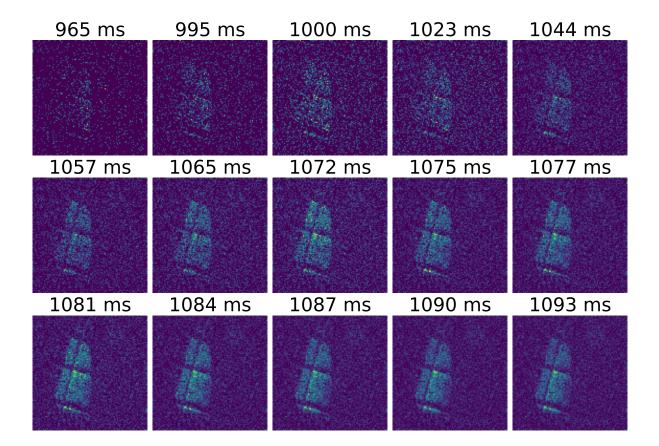
Figure 5.20: Shot 20068, first 15 out of 100 hitmaps generated from the separated time intervals. The hits are collected from the start of the shot ($\approx$ 950 ms) until the time shown in the title of the corresponding image.

Figure 5.21: Shot 20056, tiles of the tokamak limiter hit by REs. Snapshot in the optical region using the camera Photron Mini UX100. The camera framerate is 6.25 kfps.
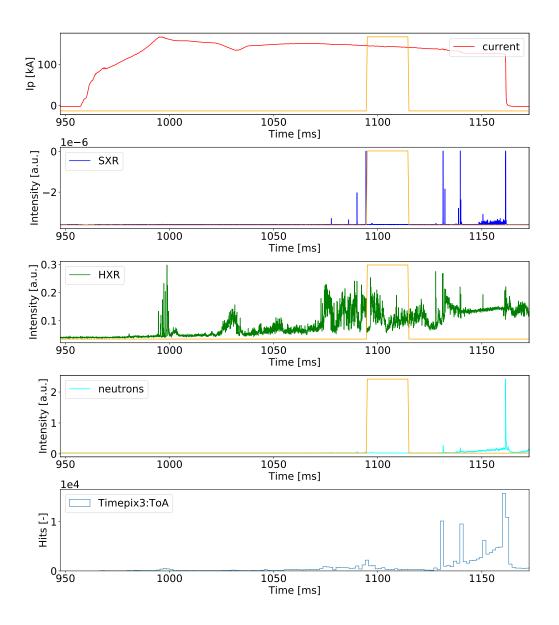
Figure 5.22: Shot 20068, the ToA signal from the Timepix3 plotted with the key RE diagnostics from the tokamak. The Ar puff is shown in orange. The shot ended with a disruption at 1161.42 ms. This is accompanied by the strong peaks in all RE diagnostics. The peak in the neutrons signal from the shielded scintillation detector probably shows, that REs reached the wall where photoneutrons were produced.
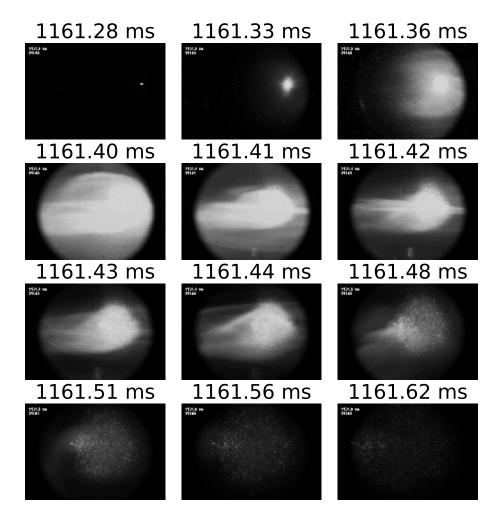
Figure 5.23: Shot 20068, the carbon pellet explosion seen by the Photron SA-X2 camera. The camera framerate is 100 kfps.

Conclusion

This work summarizes the fundamentals of the thermonuclear fusion, plasma physics and the toka-mak configuration; describes the generation mechanisms of the REs, the methods of diagnostics and strategies for mitigation of their impact on the tokamak first wall; summarizes the most important mechanisms of radiation-matter interaction on which particle detectors rely; discusses the fundamentals of the semiconductor detectors and their principles of operation. Furthermore, results obtained with the Timepix3 detector during the 11th RE dedicated campaign at the COMPASS tokamak are presented.

The Timepix3 has successfully fulfilled its purpose and showed good functionality during the experimental campaign. The ToA signal was compared with the diagnostics installed at the COMPASS tokamak, mainly scintillation detectors and a set of bolometers. Though the ToT signal was also analyzed and processed for each shot, it did not provide as much information as the ToA signals. In order to give information about the energy of the particles measured, the detector has to be delicately calibrated via charge injection and corresponding software. Such calibration should be a part of future studies. Nonetheless, the detector has shown good functionality and the work on acquiring the spectra will be continued.

As there almost no experience with operation of hybrid semiconductor detectors in the tokamak environment, the Timepix3 detector met obstacles that were gradually solved as the experiments continued. The first problem was the saturation of the detector which can occur either due to the high frequency of measured events (detection of the incoming particles) or due to the large deposited energy that the readout system cannot process. The first step to overcome this was to minimize the active window of the sensor by turning some of the pixels off. In particular shots, when the RE intensity was expected to be mild, the active window had $\approx$ 12000 pixels active; in the most intense shots, the window had $\approx$ 1600 pixels active. Despite the narrowing of the field of view, it facilitated the readout system and made possible to continue the measurements. Furthermore, as the RE intensity rose, the detector setup was supplemented with a set of lead blocks 5 cm wide (shielding was 1 block wide) that screened the sensor against the incoming radiation. In the future experiments, the detector have to be supplemented with more blocks which should allow to operate the detector with a full sensor active.

From a comparison of the ToA signals to the other tokamak diagnostics one can conclude, that the Timepix3 detector does not fall behind. The spikes in signals due to the RE beam oscillations, the final spike measured during disruptions and the post-disruption RE beam radiation - all were captured with the Timepix3 detector. Furthermore, the configuration of the sensor and the functionality of the chip makes the detector very well suited for the imaging purposes. The most interesting results were obtained during a detailed analysis of the events measured across the whole sensor - the hitmaps. In almost 30% of the shots analyzed, the tiles of the limiter installed inside the tokamak vacuum chamber were seen as they were hit by the REs. It was possible due to the low-to-mild RE intensity and the narrow active window accompanied by the shielding. The pattern is always seen at the start of the shots, when the RE intensity is at the lowest, though the image is often very unclear. The best results are presented in Chapter 5, see Figures 5.19 and 5.20.

A series of almost 150 shots was conducted during the whole campaign. However, only 49 shots were successful for the Timepix3 detector. During the first couple of days of the campaign, the detector was almost always saturated, therefore providing very little useful information. Only the most successful shots are presented and described in detail with some additional good results presented in the Appendix. The Timepix3 detector has a possibility to run with an external trigger. However, due to some technical difficulties, this was utilized only during the last day of the campaign. Nonetheless, in terms of the results achieved, this was the most successful day of the campaign. In shots, where there was no trigger connected, the ToA signal has to be manually aligned with the other diagnostics and the time axis will be different as the detector runs separately from the other systems. This makes the measurements less precise; therefore, only one such shot is presented.

In conclusion, the measurements at the COMPASS tokamak with the Timepix3 detector were successful. The results obtained have shown new possibilities for future experiments. However, the diagnostic setup still requires some improvements. The Timepix3 detector will be a part of the RE diagnostics in the future experimental campaigns.

List of Symbols

$\ln \Lambda$	Coulomb logarithm
α	index [Chapter 1],
	fit coefficient [Chapter 4]
$\boldsymbol{\beta}$	beta parameter $\boldsymbol{\beta} = \frac{\mathbf{v}}{c}$
β	index [Chapter 1],
	beta parameter $\beta = \frac{v}{c}$ [Chapter 2],
	fit coefficient [Chapter 4]
β_{Te}	electron thermal velocities
β_{Ti}	ion thermal velocity
γ	Lorentz factor [Chapter 2],
	photon [Chapter 3]
ϵ	average energy required for an electron-hole pair generation
ε	absolute material permittivity
ε_0	vacuum permittivity
λ	photon attenuation length
λ_{D}	Debye length
μ	reduced mass
μ_{n}	electron mobility
μ_{p}	hole mobility
ν	photon frequency
ν_{c}	critical photon frequency [in terms of the Compton scattering]
ν_{coll}	collision frequency
ν'	photon frequency after the Compton scattering
ρ	charge density
σ	electric conductivity
τ	mean free time
τ_0	preacceleration time
ϕ	electric field potential
χ	electron affinity
ψ	Chandrasekhar function [Chapter 2],
	Bloch wave [Chapter 4]
A	voltage amplification factor
B	magnetic field
b	collision parameter
b_0	critical collision parameter
C	capacitance
C_D	detector capacitance

C_f	feedback capacitance
C_{in}	input capacitance
c	speed of light in vacuum
D	diffusion constant
D_n	electron diffusion constant
D_p	hole diffusion constant
d	depletion region width
$\mathbf{E}$	electric field intensity
E	energy [Chapter 1,4],
	electric field intensity [Chapter 2]
E_A	acceptor energy level
E_C	conduction band energy level
E_{CH}	Connor-Hastie electric field
E_D	Dreicer's electric field [Chapter 2],
	donor level energy [Chapter 4]
E_F	Fermi level
E_V	valence band energy level
E_{crit}	critical electric field [in terms of RE generation]
E_g	band gap energy
E_i	intrinsic semiconductor Fermi level
E_{kin}	particle kinetic energy
E_{thr}	threshold energy level [in terms of electron-hole pair generation]
E_{tor}	toroidal electric field
E_v	component of the electric field in the direction of particle velocity $\mathbf{v}$
e	electron charge
$\mathbf{F}$	force
$\mathbf{F}_L$	Lorentz force
$\mathbf{F}_{drag}$	collisional drag force
$\mathbf{F}_n$	diffusion force on the electrons
$\mathbf{F}_p$	diffusion force on the holes
$\mathbf{F}_{rad}$	radiation reaction force
F	Fano factor
f	the Fermi-Dirac distribution function
f_n	the Fermi-Dirac distribution function for electrons
f_p	the Fermi-Dirac distribution function for holes
g	relative velocity $g = v_\alpha - v_\beta$
$\mathbf{H}$	magnetic field intensity
H_0	average pulse height in a detector
h	Planck constant
I	electric current
$\mathbf{j}$	current density
$\mathbf{j}_n$	electron current density
$\mathbf{j}_p$	hole current density
$\mathbf{k}$	wave vector
k_B	Boltzmann constant
M	number of electrons/holes generated in a semiconductor
m	mass

m_e	electron rest mass
m_0	particle rest mass
m^*	effective mass
m_n^*	effective mass of electrons
m_p^*	effective mass of holes
N	density of states
N_A	density of the acceptor impurities
N_C	number of states in the conduction band
N_D	density of the donor impurities
N_V	number of states in the valence band
n	neutron [Chapter 1],
	electron density [Chapter 4]
n_e	electron density
n_i	charge carrier density in an intrinsic semiconductor
n_z	ion density
P	probability
P_{br}	bremsstrahlung power
P_{cycl}	cyclotron radiation power losses
p	momentum
$\mathbf{p}_E, p_E$	electron electric dipole moment
p	hole density
p	proton
Q	charge
Q_{in}	charge collected at the electrode
R	tokamak major radius [Chpater 2]
R	energy resolution [Chapter 4]
r_e	electron radius vector [Chapter 2],
	position vector [Chapter 4]
S	(mass) stopping power
T_e	electron temperature
U_{ion}	ionization energy
V	voltage
V_{cp}	contact potential
V_{ext}	external voltage
V_{loop}	loop voltage
V_{out}	output voltage
v	velocity
v_{crit}	critical velocity [RE region]
$\mathbf{v}_n$	electron velocity
$\mathbf{v}_p$	hole velocity
$v_\perp$	particle velocity perpendicular to the magnetic field lines
x	photon distance into material
Z	atomic number
Z_{eff}	effective ion charge

List of acronyms

ADC	Analog-to-Digital Converter
ASIC	Application Specific Integrated Circuit
CERN	Conseil Européen pour la Recherche Nucléaire (European Organization for Nuclear Research)
CMOS	Complementary Metal-Oxide-Semiconductor
COMPASS	COMPact ASSembly
CQ	Current Quench
CSA	Charge-Sensitive Amplifier
CSDA	Continuous Slowing Down Approximation [range]
DAC	Digital-to-Analog Converter
DMS	Disruption Mitigation System
D-T, **D-D**	deuterium-tritium, deuterium-deuterium [reaction]
ECE	Electron Cyclotron Emission
ECRH	Electron Cyclotron Resonant Heating
FPGA	Field-Programmable Gate Array
FTU	Frascati Tokamak Upgrade
FWHM	Full Width at Half Maximum
HFS	High Field Side
HXR	Hard X-Ray
ICF	Inertial Confinement Fusion
ICRH	Ion Cyclotron Resonant Heating
ITER	International Thermonuclear Experimental Reactor
ITPA	International Tokamak Physics Activity
JET	Joint European Torus
LFS	Low Field Side
LHCD	Lower Hybrid Current Drive
MCF	Magnetic Confinement Fusion
MGI	Massive Gas Injection
MHD	MagnetoHydroDynamics
MagLIF	Magnetized Liner Inertial Fusion
NBI	Neutral Beam Injection
PC	Personal Computer
RE	Runaway Electron
SPI	Shattered Pellet Injection
SXR	Soft X-Ray
TEXTOR	Tokamak Experiment for Technology Oriented Research
TQ	Thermal Quench
ToA	Time-of-Arrival

ToT   Time-over-Threshold

Bibliography

[1] F. Rosch, "Nuclear transformations and radioactive emissions: Part I - primary transformation pathways of unstable nuclei.," *ChemTexts*, vol. 4, no. 13, 2018. DOI:https://doi.org/10.1007/s40828-018-0068-x.

[2] J. Mlynar, "Úvod do termojaderné fúze: Fúzní jaderné reakce." https://physics.fjfi.cvut.cz/files/fttf/predmety/02UFU/utf_1_reakce.ppt, Accessed 19.3.2020.

[3] Wikipedia, "Iron-56." https://en.wikipedia.org/wiki/Iron-56, Accessed 25.3.2020.

[4] Comprehensive Nuclear-Test-Ban Treaty Organisation, "1 november 1952 - Ivy Mike." https://www.ctbto.org/specials/testing-times/1-november-1952-ivy-mike, Accessed 16.3.2020.

[5] A. Singh, "Ivy Mike: How to wipe out an island." http://large.stanford.edu/courses/2015/ph241/singh-a1/, Accessed 16.3.2020.

[6] E. Fantoni, "Nuclear island: The secret post-WWII mega lab investigated." https://www.wired.co.uk/article/nuclear-island, Accessed 16.3.2020.

[7] The ITER Organisation, "August 1968: A revolution in fusion." https://www.iter.org/newsline/43/707, Accessed 16.3.2020.

[8] S. Charley, "How to make an element." https://www.pbs.org/wgbh/nova/article/make-an-element/, Accessed 17.3.2020.

[9] M. Salaris and S. Cassisi, "Evolution of stars and stellar populations," 2008. ISBN: 978-0470092200.

[10] I. Langmuir, "Oscillations in ionized gases," *Proceedings of the National Academy of Sciences*, vol. 14, no. 8, pp. 627–637, 1928. https://www.pnas.org/content/14/8/627, Accessed 20.3.2020.

[11] D. Sinars, "Magnetized liner inertial fusion on the 100-ns Z facility and prospects of a "breakeven" experiment." https://www.arpa-e.energy.gov/sites/default/files/documents/files/Drivers_Fusion_Sinars_Presentation.pdf, Accessed 17.3.2020.

[12] T. S. Pedersen, R. König, M. Krychowiak, M. Jakubowski, J. Baldzuhn, S. Bozhenkov, G. Fuchert, A. Langenberg, H. Niemann, D. Zhang, and et al., "First results from divertor operation in Wendelstein 7-x," *Plasma Physics and Controlled Fusion*, vol. 61, no. 1, p. 014035, 2018.

[13] T. Klinger and et al., "Overview of the first Wendelstein 7-x high-performance operation," *Nuclear Fusion*, vol. 59, p. 112004, jun 2019.

[14] The ITER Organisation, "Magnets." `https://www.iter.org/mach/Magnets`, Accessed 17.3.2020.

[15] E. Westerhof, "Non-inductive current drive." `https://core.ac.uk/download/pdf/35070401.pdf`, Accessed 28.04.2020.

[16] J. Decker, Y. Peysson, J. Hillairet, J.-F. Artaud, V. Basiuk, A. Becoulet, A. Ekedahl, M. Goniche, G. Hoang, F. Imbeaux, A. Ram, and M. Schneider, "Calculations of lower hybrid current drive in ITER," *Nuclear Fusion*, vol. 51, p. 073025, jun 2011.

[17] K. Sakamoto and et. al., "Progress in ITER heating and current drive system." `https://www-pub.iaea.org/MTCD/Meetings/FEC2008/it_2-1.pdf`, Accessed 17.3.2020.

[18] P. Kulhánek, "Úvod do teorie plazmatu," 2011. ISBN: 678-80-904582-2-2.

[19] S. Li, H. Jiang, Z. Ren, and C. Xu, "Optimal Tracking for a Divergent-Type Parabolic PDE System in Current Profile Control," *Abstract and Applied Analysis*. `https://doi.org/10.1155/2014/940965`, Accessed 25.03.2020.

[20] A. S. Richardson, "Naval Research Laboratory plasma formulary." `https://www.nrl.navy.mil/ppd/sites/www.nrl.navy.mil.ppd/files/pdfs/NRL_Formulary_2019.pdf`, Accessed 17.3.2020.

[21] Health Physics Society, "Tritium: Fact Sheet." `https://hps.org/documents/tritium_fact_sheet.pdf`, Accessed 28.04.2020.

[22] The ITER Organisation, "Fuelling the fusion reaction." `https://www.iter.org/sci/FusionFuels`, Accessed 17.3.2020.

[23] International Atomic Energy Agency, "Evaluated nuclear data file database." `https://www-nds.iaea.org/exfor/endf.htm`, Accessed, 2.06.2020.

[24] "Lithium: isotope data." `https://www.webelements.com/lithium/isotopes.html`, Accessed 11.7.2020.

[25] N. Zandi, H. Sadeghi, M. Habibi, I. Jalali, and M. Zare, "Blanket simulation and tritium breeding ratio calculationfor ITER reactor." DOI: https://doi.org/10.1007/s10894-015-9970-z.

[26] The ITER Organisation, "What will iter do?." `https://www.iter.org/sci/Goals`, Accessed 17.3.2020.

[27] The ITER Organisation, "External heating." `https://www.iter.org/mach/Heating`, Accessed 17.3.2020.

[28] The ITER Organisation, "Tritium breeding." `https://www.iter.org/mach/TritiumBreeding`, Accessed 17.3.2020.

[29] The ITER Organisation, "First plasma: 2025." `https://www.iter.org/mag/9/65`, Accessed 23.3.2020.

[30] G. Kalinin, V. Barabash, A. Cardella, J. Dietz, K. Ioki, R. Matera, R. Santoro, and R. Tivey, "Assessment and selection of materials for iter in-vessel components," *Journal of Nuclear Materials*, vol. 283-287, p. 10–19, 2000.

[31] J. Wesson and D. J. Campbell, "Tokamaks," 2011. ISBN: 9780199592234.

[32] C. T. R. Wilson, "The electric field of a thundercloud and some of its effects," *Proceedings of the Physical Society of London*, vol. 37, pp. 32D–37D, jan 1924. `https://doi.org/10.1088%2F1478-7814%2F37%2F1%2F314`, Accessed 22.3.2020.

[33] R. Jaspers, "Relativistic runaway electrons in tokamak plasmas," 1995.

[34] V. A. Delong, R. Beňo, D. Břeň, and P. Kulhánek, "Notes on the relativistic movement of runaway electrons in parallel electric and magnetic fields," *Physics of Plasmas*, vol. 23, no. 9, p. 094504, 2016. `https://doi.org/10.1063/1.4962687`, Accessed 20.3.2020.

[35] W. Pauli, "Theory of Relativity," 1958.

[36] P. Kulhánek, "Vybrané kapitoly z fyziky plazmatu," 2017.

[37] B. Carlson, "Runaway electrons." `https://en.wikipedia.org/wiki/Relativistic_runaway_electron_avalanche#/media/File:Runaway_electron_dynamic_friction_in_air.svg` Accessed 18.3.2020.

[38] B. N. Breizman, P. Aleynikov, E. M. Hollmann, and M. Lehnen, "Physics of runaway electrons in tokamaks," *Nuclear Fusion*, vol. 59, no. 8, p. 083001, 2019.

[39] N. S. Khaerdinov and A. S. Lidvansky, "Heights of generation of runaway electrons in bright cosmic ray events observed on the ground during thunderstorms," *Journal of Physics: Conference Series*, vol. 409, p. 012225, Jan 2013.

[40] H. Dreicer, "Electron and ion runaway in a fully ionized gas. ii," *Physical Review*, vol. 117, no. 2, p. 329–342, 1960. `https://doi.org/10.1103/PhysRev.117.329`, Accessed 23.3.2020.

[41] J. Connor and R. Hastie, "Relativistic limitations on runaway electrons," *Nuclear Fusion*, vol. 15, p. 415–424, Jan 1975.

[42] R. Granetz, B. Esposito, J. Kim, R. Koslowski, M. Lehnen, J. Martin-Solis, C. Paz-Soldan, T. Rhee, J. Wesley, and L. Zeng, "An ITPA joint experiment to study runaway electron generation and suppression," *Physics of Plasmas*, vol. 21, p. 072506, 07 2014.

[43] J. R. Martín-Solís, R. Sánchez, and B. Esposito, "Experimental observation of increased threshold electric field for runaway generation due to synchrotron radiation losses in the ftu tokamak," *Phys. Rev. Lett.*, vol. 105, p. 185002, Oct 2010. `https://link.aps.org/doi/10.1103/PhysRevLett.105.185002`, Accessed 20.3.2020.

[44] F. C. Schuller, "Disruptions in tokamaks," *Plasma Physics and Controlled Fusion*, vol. 37, Jan 1995.

[45] H. M. Smith and E. Verwichte, "Hot tail runaway electron generation in tokamak disruptions," *Physics of Plasmas*, vol. 15, no. 7, p. 072502, 2008.

[46] M. Rosenbluth and S. Putvinski, "Theory for avalanche of runaway electrons in tokamaks," *Nuclear Fusion*, vol. 37, no. 10, p. 1355–1362, 1997.

[47] Z. Popovic, B. Esposito, J. R. Martín-Solís, W. Bin, P. Buratti, D. Carnevale, F. Causa, M. Gospodarczyk, D. Marocco, G. Ramogida, and M. Riva, "On the measurement of the threshold electric field for runaway electron generation in the frascati tokamak upgrade," *Physics of Plasmas*, vol. 23, no. 12, p. 122501, 2016. `https://doi.org/10.1063/1.4968839`, Accessed 21.3.2020.

[48] O. Ficker, "Generation, losses and detection of runaway electrons in tokamaks," Master's thesis, 2015.

[49] H. Knoepfel and D. Spong, "Runaway electrons in toroidal discharges," *Nuclear Fusion*, vol. 19, pp. 785–829, jun 1979. `https://doi.org/10.1088%2F0029-5515%2F19%2F6%2F008`, Accessed 21.3.2020.

[50] J. Mlynar, O. Ficker, M. Vlainic, V. Weinzettl, M. Imrisek, R. Paprok, M. Rabinski, M. Jakubowski, M. Tomes, M. Peterka, and R. Panek, "Effects of plasma control on runaway electrons in the compass tokamak," *42nd EPS Conference on Plasma Physics*. `http://ocs.ciemat.es/EPS2015PAP/pdf/P4.102.pdf`, Accessed 30.3.2020.

[51] T. Fehér, H. M. Smith, T. Fülöp, and K. Gál, "Simulation of runaway electron generation during plasma shutdown by impurity injection in ITER," *Plasma Physics and Controlled Fusion*, vol. 53, p. 035014, feb 2011. `https://doi.org/10.1088%2F0741-3335%2F53%2F3%2F035014`, Accessed 21.3.2020.

[52] E. M. Hollmann, P. B. Aleynikov, T. Fülöp, D. A. Humphreys, V. A. Izzo, M. Lehnen, V. E. Lukash, G. Papp, G. Pautasso, F. Saint-Laurent, and J. A. Snipes, "Status of research toward the iter disruption mitigation system," *Physics of Plasmas*, vol. 22, no. 2, p. 021802, 2015. `https://doi.org/10.1063/1.4901251`, Accessed 21.3.2020.

[53] E. Hollmann, P. Parks, N. Commaux, N. Eidietis, R. Moyer, D. Shiraki, M. Austin, C. Lasnier, C. Paz-Soldan, and D. Rudakov, "Measurement of runaway electron energy distribution function during high-z gas injection into runaway electron plateaus in diii-d," *Physics of Plasmas*, vol. 22, p. 056108, 05 2015.

[54] A. H. Boozer, "Runaway electrons and iter," *Nuclear Fusion*, vol. 57, no. 5, p. 056018, 2017.

[55] Z. Y. Chen, W. C. Kim, Y. W. Yu, A. C. England, J. W. Yoo, S. H. Hahn, S. W. Yoon, K. D. Lee, Y. K. Oh, J. G. Kwak, and M. Kwon, "Study of runaway current generation following disruptions in KSTAR," *Plasma Physics and Controlled Fusion*, vol. 55, p. 035007, feb 2013. `https://doi.org/10.1088%2F0741-3335%2F55%2F3%2F035007`, Accessed 21.3.2020.

[56] R. Jayakumar, H. Fleischmann, and S. Zweben, "Collisional avalanche exponentiation of run-away electrons in electrified plasmas," Jan 1992.

[57] T. Hender, J. Wesley, J. Bialek, A. Bondeson, A. Boozer, R. Buttery, A. Garofalo, T. Goodman, R. Granetz, Y. Gribov, O. Gruber, M. Gryaznevich, G. Giruzzi, S. Günter, N. Hayashi, P. Helander, C. Hegna, D. Howell, D. Humphreys, G. Huysmans, A. Hyatt, A. Isayama, S. Jardin, Y. Kawano, A. Kellman, C. Kessel, H. Koslowski, R. L. Haye, E. Lazzaro, Y. Liu, V. Lukash, J. Manickam, S. Medvedev, V. Mertens, S. Mirnov, Y. Nakamura, G. Navratil, M. Okabayashi, T. Ozeki, R. Paccagnella, G. Pautasso, F. Porcelli, V. Pustovitov, V. Riccardo, M. Sato, O. Sauter, M. Schaffer, M. Shimada, P. Sonato, E. Strait, M. Sugihara, M. Takechi, A. Turnbull, E. Westerhof, D. Whyte, R. Yoshino, H. Zohm, D. the ITPA MHD, and M. Group, "Chapter 3:

MHD stability, operational limits and disruptions," *Nuclear Fusion*, vol. 47, pp. S128–S202, jun 2007. `https://doi.org/10.1088%2F0029-5515%2F47%2F6%2Fs03`, Accessed 19.3.2020.

[58] M. Hoppe, O. Embréus, R. Tinguely, R. Granetz, A. Stahl, and T. Fülöp, "SOFT: a synthetic synchrotron diagnostic for runaway electrons," *Nuclear Fusion*, vol. 58, p. 026032, jan 2018. `https://doi.org/10.1088%2F1741-4326%2Faa9abb`, Accessed 20.3.2020.

[59] M. Hoppe, O. Embréus, C. Paz-Soldan, R. Moyer, and T. Fülöp, "Interpretation of runaway electron synchrotron and bremsstrahlung images," *Nuclear Fusion*, vol. 58, p. 082001, jun 2018. `https://doi.org/10.1088%2F1741-4326%2Faaae15`, Accessed 20.3.2020.

[60] C. Paz-Soldan, C. M. Cooper, P. Aleynikov, D. C. Pace, N. W. Eidietis, D. P. Brennan, R. S. Granetz, E. M. Hollmann, C. Liu, A. Lvovskiy, R. A. Moyer, and D. Shiraki, "Spatiotemporal evolution of runaway electron momentum distributions in tokamaks," *Phys. Rev. Lett.*, vol. 118, p. 255002, Jun 2017. `https://link.aps.org/doi/10.1103/PhysRevLett.118.255002`, Accessed 22.3.2020.

[61] R. Tinguely, R. Granetz, M. Hoppe, and O. Embréus, "Measurements of runaway electron synchrotron spectra at high magnetic fields in alcator c-mod," *Nuclear Fusion*, vol. 58, p. 076019, jun 2018. `https://doi.org/10.1088%2F1741-4326%2Faac444`, Accessed 21.3.2020.

[62] E. Hollmann, M. Austin, J. Boedo, N. Brooks, N. Commaux, N. Eidietis, D. Humphreys, V. Izzo, A. James, T. Jernigan, A. Loarte, J. Martin-Solis, R. Moyer, J. Muñoz-Burgos, P. Parks, D. Rudakov, E. Strait, C. Tsui, M. V. Zeeland, J. Wesley, and J. Yu, "Control and dissipation of runaway electron beams created during rapid shutdown experiments in DIII-d," *Nuclear Fusion*, vol. 53, p. 083004, jul 2013. `https://doi.org/10.1088%2F0029-5515%2F53%2F8%2F083004`, Accessed 23.3.2020.

[63] S. Kulkov, "Runaway electrons and their detection using segmented silicon detectors," *Research Project*, 2019. `https://physics.fjfi.cvut.cz/publications/FTTF/VU_Sergei_Kulkov.pdf` Accessed 01.04.2020.

[64] M. Forster, K. H. Finken, M. Lehnen, O. Willi, and Y. a. Xu, "Measurements of the runaway electron energy during disruptions in the tokamak textor," *Physics of Plasmas*, vol. 19, no. 5, p. 052506, 2012.

[65] M. Farnik, J. Urban, J. Zajac, O. Bogar, O. Ficker, E. Macusova, J. Mlynar, J. Cerovsky, M. Varavin, V. Weinzettl, and et al., "Runaway electron diagnostics for the compass tokamak using ec emission," *EPJ Web of Conferences*, vol. 203, p. 03006, 2019.

[66] C. Liu, L. Shi, E. Hirvijoki, D. P. Brennan, A. Bhattacharjee, C. Paz-Soldan, and M. E. Austin, "The effects of kinetic instabilities on the electron cyclotron emission from runaway electrons," *Nuclear Fusion*, vol. 58, p. 096030, Dec 2018.

[67] L. Jakubowski, M. J. Sadowski, J. Zebrowski, K. Malinowski, M. Rabinski, M. J. Jakubowski, and R. Mirowski, "Cherenkov-type diagnostics of fast electrons within tokamak plasmas," *Physica Scripta*, vol. T161, p. 014011, may 2014. `https://doi.org/10.1088%2F0031-8949%2F2014%2Ft161%2F014011`, Accessed 21.3.2020.

[68] J. Zebrowski, L. Jakubowski, M. Rabinski, M. J. Sadowski, M. J. Jakubowski, R. Kwiatkowski, K. Malinowski, R. Mirowski, J. Mlynar, O. Ficker, V. Weinzettl, F. Causa, and and, "Studies of runaway electrons via cherenkov effect in tokamaks," *Journal of Physics: Conference Series*, vol. 959, p. 012002, jan 2018. `https://doi.org/10.1088%2F1742-6596%2F959%2F1%2F012002`, Accessed 23.3.2020.

[69] M. Lehnen, S. Abdullaev, G. Arnoux, S. Bozhenkov, M. Jakubowski, R. Jaspers, V. Plyusnin, V. Riccardo, and U. Samm, "Runaway generation during disruptions in jet and textor," *Journal of Nuclear Materials*, vol. 390-391, pp. 740 – 746, 2009. Proceedings of the 18th International Conference on Plasma-Surface Interactions in Controlled Fusion Device.

[70] E. M. Hollmann, N. Commaux, N. W. Eidietis, C. J. Lasnier, D. L. Rudakov, D. Shiraki, C. Cooper, J. R. Martin-Solis, P. B. Parks, and C. Paz-Soldan, "Study of z scaling of runaway electron plateau final loss energy deposition into wall of diii-d," *Physics of Plasmas*, vol. 24, no. 6, p. 062505, 2017. `https://doi.org/10.1063/1.4985086`, Accessed 22.3.2020.

[71] J. Mlynar, O. Ficker, E. Macusova, T. Markovic, D. Naydenkova, G. Papp, J. Urban, M. Vlainic, P. Vondracek, V. Weinzettl, O. Bogar, D. Bren, D. Carnevale, A. Casolari, J. Cerovsky, M. Farnik, M. Gobbin, M. Gospodarczyk, M. Hron, P. Kulhanek, J. Havlicek, A. Havranek, M. Imrisek, M. Jakubowski, N. Lamas, V. Linhart, K. Malinowski, M. Marcisovsky, E. Matveeva, R. Panek, V. V. Plyusnin, M. Rabinski, V. Svoboda, P. Svihra, J. Varju, and J. Z. and, "Runaway electron experiments at COMPASS in support of the EUROfusion ITER physics research," *Plasma Physics and Controlled Fusion*, vol. 61, p. 014010, nov 2018. `https://doi.org/10.1088%2F1361-6587%2Faae04a`, Accessed 21.3.2020.

[72] L. Baylor, C. C. Barbier, J. R. Carmichael, S. K. Combs, M. N. Ericson, N. D. B. Ezell, P. W. Fisher, M. S. Lyttle, S. J. Meitner, D. A. Rasmussen, and et al., "Disruption mitigation system developments and design for iter," *Fusion Science and Technology*, vol. 68, no. 2, p. 211–215, 2015.

[73] E. M. Hollmann, P. B. Aleynikov, T. Fülöp, D. A. Humphreys, V. A. Izzo, M. Lehnen, V. E. Lukash, G. Papp, G. Pautasso, F. Saint-Laurent, and J. A. Snipes, "Status of research toward the iter disruption mitigation system," *Physics of Plasmas*, vol. 22, no. 2, p. 021802, 2015. `https://doi.org/10.1063/1.4901251`, Accessed 25.3.2020.

[74] M. Lehnen and S. Maruyama, "ITER Disruption Mitigation Workshop, ITER HQ, 8 – 10 March 2017." `https://www.iter.org/doc/www/content/com/Lists/ITER%20Technical%20Reports/Attachments/8/ITER_Disruption_Mitigation_Workshop.pdf`, Accessed 1.04.2020.

[75] M. Lehnen, G. Arnoux, S. Brezinsek, J. Flanagan, S. Gerasimov, N. Hartmann, T. Hender, A. Huber, S. Jachmich, V. Kiptily, and et al., "Impact and mitigation of disruptions with the iter-like wall in jet," *Nuclear Fusion*, vol. 53, p. 093007, Sep 2013.

[76] N. Commaux, L. Baylor, T. Jernigan, E. Hollmann, P. Parks, D. Humphreys, J. Wesley, and J. Yu, "Demonstration of rapid shutdown using large shattered deuterium pellet injection in diii-d," *Nuclear Fusion*, vol. 50, p. 112001, Aug 2010.

[77] M. Lehnen, S. A. Bozhenkov, S. S. Abdullaev, and M. W. Jakubowski, "Suppression of runaway electrons by resonant magnetic perturbations in textor disruptions," *Phys. Rev. Lett.*, vol. 100,

p. 255003, Jun 2008. `https://link.aps.org/doi/10.1103/PhysRevLett.100.255003`, Accessed 20.3.2020.

[78] N. Commaux, L. Baylor, S. Combs, N. Eidietis, T. Evans, C. Foust, E. Hollmann, D. Humphreys, V. Izzo, A. James, T. Jernigan, S. Meitner, P. Parks, J. Wesley, and J. Yu, "Novel rapid shutdown strategies for runaway electron suppression in DIII-d," *Nuclear Fusion*, vol. 51, p. 103001, aug 2011. `https://doi.org/10.1088%2F0029-5515%2F51%2F10%2F103001`, Accessed 21.3.2020.

[79] B. Esposito and et al., "Runaway generation and control." `http://www.euro-fusionscipub.org/wp-content/uploads/WPMST2CP16_15344_submitted.pdf`, Accessed 21.3.2020.

[80] N. W. Eidietis, N. Commaux, E. M. Hollmann, D. A. Humphreys, T. C. Jernigan, R. A. Moyer, E. J. Strait, M. A. VanZeeland, J. C. Wesley, and J. H. Yu, "Control of post-disruption runaway electron beams in diii-d," *Physics of Plasmas*, vol. 19, no. 5, p. 056109, 2012. `https://doi.org/10.1063/1.3695000`, Accessed 25.3.2020.

[81] M. Bakhtiari, G. J. Kramer, M. Takechi, H. Tamai, Y. Miura, Y. Kusama, and Y. Kamada, "Role of bremsstrahlung radiation in limiting the energy of runaway electrons in tokamaks," *Phys. Rev. Lett.*, vol. 94, p. 215003, Jun 2005. `https://link.aps.org/doi/10.1103/PhysRevLett.94.215003`, Accessed 20.3.2020.

[82] A. Stahl, M. Landreman, G. Papp, E. Hollmann, and T. Fulop, "Synchrotron radiation from a runaway electron distribution in tokamaks." DOI: 10.1063/1.4821823.

[83] L. L. Gunderson and J. E. Tepper, "Clinical radiation oncology," 2015. ISBN: 978-0323240987.

[84] S. N. Ahmed, "Physics and Engineering of Radiation Detection," 2015. DOI: https://doi.org/10.1016/C2013-0-15270-1.

[85] National Institute of Standards and Technology, "Cross-section for the photon-silicon interaction." `https://physics.nist.gov/cgi-bin/Xcom/xcom2?Method=Elem&Output2=File&elNum=6&elName=Carbon&elSymbol=C`, Accessed 20.3.2020.

[86] O. Jarvis, G. Sadler, and J. Thompson, "Photoneutron production accompanying plasma disruptions in JET," *Nuclear Fusion*, vol. 28, pp. 1981–1993, nov 1988.

[87] The ITER Organisation, "Blanket." `https://www.iter.org/mach/Blanket`, Accessed 22.3.2020.

[88] J. Bielecki and A. Kurowski, "Neutron diagnostics for tokamak plasma: From a plasma diagnostician perspective," `https://link.springer.com/article/10.1007/s10894-018-0195-9#citeas`, Accessed 22.3.2020.

[89] M. Kovari, C. Harrington, I. Jenkins, and C. Keily, "Converting energy from fusion into useful forms." `https://arxiv.org/pdf/1401.4232.pdf`, Accessed 21.3.2020.

[90] NIST, "Stopping power and range tables for electrons." `https://physics.nist.gov/PhysRefData/Star/Text/ESTAR.html`, Accessed 21.3.2020.

[91] P. Sigmund, "Particle penetration and radiation effects," 2016. ISBN: 978-3-540-31718-0.

[92] H. Gumus and A. Bentabet, "Csda range, stopping power and mean penetration depth energy relationships in some hydrocarbons and biologic materials for 10 ev to 100 mev with the modified rohrlich–carlson model," *Applied Physics A*, vol. 123, 04 2017.

[93] B. Henke, E. Gullikson, and J. Davis, "X-ray attenuation length." `http://henke.lbl.gov/optical_constants/atten2.html`, Accessed 21.3.2020.

[94] G. F. Knoll, "Radiation detection and measurement," 2000. ISBN: 0-471-07338-5.

[95] C. Bera, "Thermo electric properties of nanocomposite materials," 10 2010.

[96] C. Kittel, *Introduction to Solid State Physics*. John Wiley & Sons, Inc, 2005.

[97] M. Mazziotta, "Electron–hole pair creation energy and Fano factor temperature dependence in silicon," *Nuclear Instruments and Methods in Physics Research Section A: Accelerators, Spectrometers, Detectors and Associated Equipment*, vol. 584, no. 2, pp. 436 – 439, 2008. `http://www.sciencedirect.com/science/article/pii/S0168900207022668`, Accessed 28.4.2020.

[98] Y. Varshni, "Temperature dependence of the energy gap in semiconductors," *Physica*, vol. 34, no. 1, pp. 149 – 154, 1967. `http://www.sciencedirect.com/science/article/pii/0031891467900626`, Accessed 8.4.2020.

[99] F. Lappe, "The energy of electron-hole pair formation by X-rays in PbO," *Journal of Physics and Chemistry of Solids*, vol. 20, no. 3, pp. 173 – 176, 1961. `http://www.sciencedirect.com/science/article/pii/0022369761900014`, Accessed 27.4.2020.

[100] C. A. Klein, "Bandgap dependence and related features of radiation ionization energies in semiconductors," *Journal of Applied Physics*, vol. 39, no. 4, pp. 2029–2038, 1968. `https://doi.org/10.1063/1.1656484`, Accessed 27.4.2020.

[101] R. C. Alig and S. Bloom, "Electron-hole-pair creation energies in semiconductors," *Phys. Rev. Lett.*, vol. 35, pp. 1522–1525, Dec 1975. `https://link.aps.org/doi/10.1103/PhysRevLett.35.1522`, Accessed 28.4.2020.

[102] N. W. Ashcroft and N. D. Mermin, *Solid State Physics*. Saunders College Publishing, 1976.

[103] S. M. Sze and M. K. Lee, *Semiconductor Devices: Physics and Technology*. John Wiley & Sons, Inc, 1985.

[104] G. Lutz, "Semiconductor radiation detectors: device physics," 2007. ISBN: 978-3-540-71679-2.

[105] T. Goudon, V. Miljanovic, and C. Schmeiser, "On the shockley-read-hall model: Generation-recombination in semiconductors," *SIAM Journal of Applied Mathematics*, vol. 67, pp. 1183–1201, 01 2007.

[106] B. V. Zeghbroeck, "Semiconductor Fundamentals," 2011. `https://ecee.colorado.edu/~bart/book/book/chapter2/ch2_8.htm`, Accessed 8.4.2020.

[107] Wikipedia, "p-n junction."
`https://en.wikipedia.org/wiki/P\T1\textendash n_junction`, Accessed 26.4.2020.

[108] B. V. Zeghbroeck, "p-n junctions," 2011.
`https://ecee.colorado.edu/~bart/book/book/toc4.htm`, Accessed 8.4.2020.

[109] Computer History Museum, "1940: Discovery of the p-h junction." `https://www.computerhistory.org/siliconengine/discovery-of-the-p-n-junction/`, Accessed 18.6.2020.

[110] L. Rossi, P. Fischer, T. Rohe, and N. Wermes, *Pixel Detectors.* Springer, 2006.

[111] W. Shockley, "Currents to conductors induced by a moving point charge," *Journal of Applied Physics*, vol. 9, no. 10, pp. 635–636, 1938. DOI:`https://doi.org/10.1063/1.1710367`.

[112] S. Ramo, "Currents induced by electron motion," *Proceedings of the IRE*, vol. 27, no. 9, pp. 584–585, 1939. DOI:`https://doi.org/10.1109/JRPROC.1939.228757`.

[113] Z. He, "Review of the shockley–ramo theorem and its application in semiconductor gamma-ray detectors," *Nuclear Instruments and Methods in Physics Research Section A: Accelerators, Spectrometers, Detectors and Associated Equipment*, vol. 463, no. 1, pp. 250 – 267, 2001. DOI: `https://doi.org/10.1016/S0168-9002(01)00223-6`.

[114] C. Cottini, E. Gatti, G. Giannelli, and et al., "Minimum noise pre-amplifier for fast ionization chambers," *Nuovo Cimento*, vol. 3, pp. 473–483, 1956. DOI: `https://doi.org/10.1007/BF02745432`.

[115] K. S. Tadashi Orita, Mizuki Uenomachi, "Development of Time-over-Threshold ASICs for radiation sensors." `https://indico.cern.ch/event/669866/contributions/3227838/attachments/1770723/2877198/Poster_ToTASIC_181204.pdf`, Accessed 10.4.2020.

[116] L. Tlustos and E. Heijne, "Performance and limitations of high granularity single photon processing x-ray imaging detectors," 01 2005.

[117] B. van der Heijden, J. Visser, M. van Beuzekom, H. Boterenbrood, S. Kulis, B. Munneke, and F. Schreuder, "SPIDR, a general-purpose readout system for pixel ASICs," *Journal of Instrumentation*, vol. 12, pp. C02040–C02040, feb 2017. `https://doi.org/10.1088%2F1748-0221%2F12%2F02%2Fc02040`, Accessed 29.4.2020.

[118] Z. Janoska, M. Carna, M. Havranek, M. Hejtmanek, V. Kafka, M. Marcisovsky, G. Neue, L. Tomasek, and V. Vrba, "Measurement of ionizing particles by the ph32 chip," pp. 1–5, 10 2015.

[119] M. Havranek, T. Benka, M. Hejtmanek, Z. Janoska, D. Lednicky, V. Kafka, M. Marcisovska, M. Marcisovsky, G. Neue, P. Svihra, L. Tomasek, P. Vancura, and V. Vrba, "X-chip-03: Soi maps radiation sensor with hit-counting and adc mode," pp. 1–4, 11 2018.

[120] T. Poikela, J. Plosila, T. Westerlund, M. Campbell, M. D. Gaspari, X. Llopart, V. Gromov, R. Kluit, M. van Beuzekom, F. Zappon, V. Zivkovic, C. Brezina, K. Desch, Y. Fu, and A. Kruth, "Timepix3: a 65k channel hybrid pixel readout chip with simultaneous ToA/ToT and sparse readout," *Journal of Instrumentation*, vol. 9, pp. C05013–C05013, may 2014.

[121] J. Visser, M. van Beuzekom, H. Boterenbrood, B. van der Heijden, J. Muñoz, S. Kulis, B. Munneke, and F. Schreuder, "SPIDR: a read-out system for Medipix3 & Timepix3," *Journal of Instrumentation*, vol. 10, pp. C12028–C12028, dec 2015. `https://doi.org/10.1088%2F1748-0221%2F10%2F12%2Fc12028`, Accessed 29.4.2020.

[122] CERN, "Timepix3." `https://kt.cern/success-stories/medipix-chips-and-collaborations-medical-imaging-space-dosimetry`, Accessed 11.4.2020.

[123] R. Panek, O. Bilykova, V. Fuchs, M. Hron, P. Chraska, P. Pavlo, J. Stockel, J. Urban, V. Weinzettl, J. Zajac, and F. Zacek, "Reinstallation of the COMPASS-D Tokamak in IPP ASCR," `https://www.aldebaran.cz/bulletin/2006_20/386_1.pdf`, Accessed 5.5.2020.

[124] "JET: EUROfusion's flagship device." `https://www.euro-fusion.org/devices/jet/`, Accessed 27.2.2020.

[125] "ASDEX Upgrade." `https://www.ipp.mpg.de/16195/asdex`, Accessed 27.7.2020.

[126] Institute of Plasma Physics, "COMPASS Tokamak." `http://www.ipp.cas.cz/vedecka_struktura_ufp/tokamak/tokamak_compass/`, Accessed 5.5.2020.

[127] A. Jiri, "Compass tokamak chamber." `https://commons.wikimedia.org/wiki/File:COMPASStokamak_chamber.jpg`, Accessed 22.6.2020.
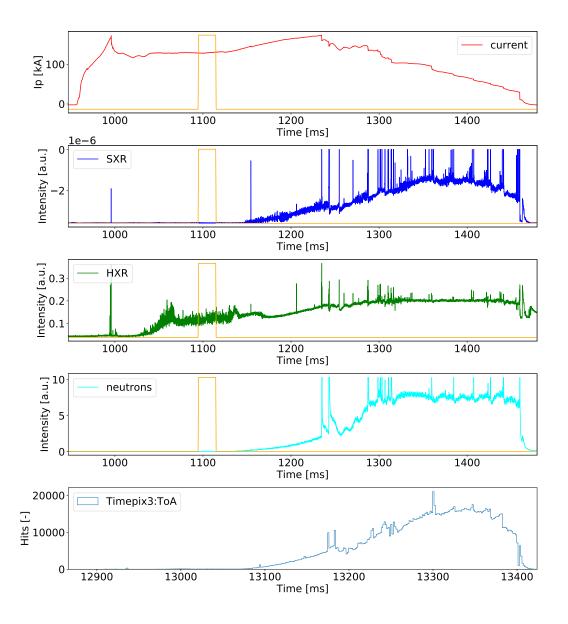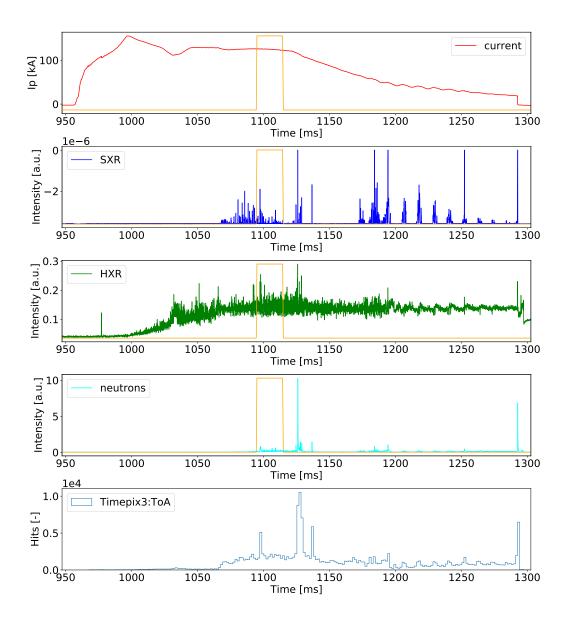
Appendix

Figure 1: Shot 20032, the ToA signal from the Timepix3 plotted with the key diagnostics from the tokamak. The Ar puff is shown in orange. The Timepix3 operated with ≈ 1600 pixels active and without a trigger - the signal alignment with the tokamak diagnostics was conducted manually. The oscillations in all signals are given by the RE beam oscillation and the enduring neutron signal is given by the RE beam instability that continuously lead to a contact between the REs and the first wall.
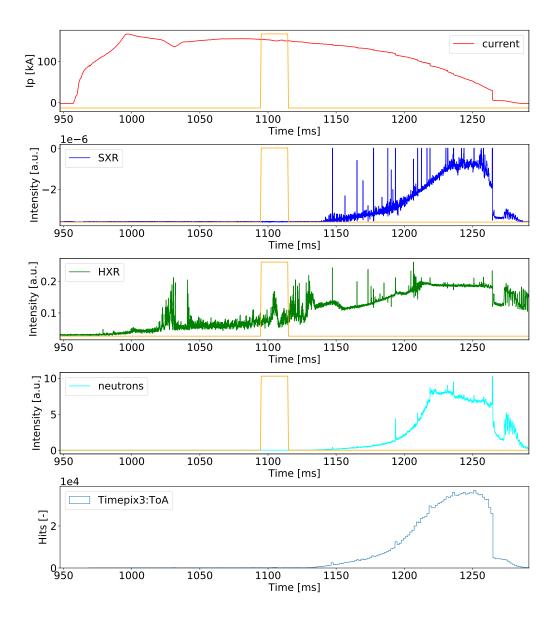
Figure 2: Shot 20056, the ToA signal from the Timepix3 plotted with the key diagnostics from the tokamak. The Ar puff is shown in orange. The Timepix3 operated with ≈ 1600 pixels active. The oscillations in all signals are given by the RE beam oscillation.
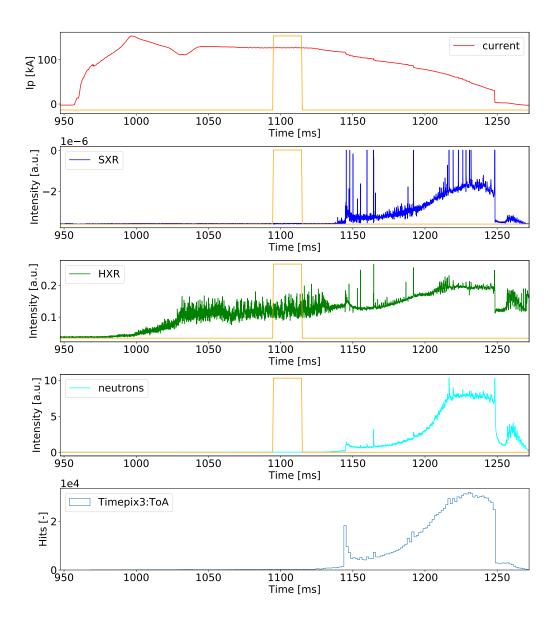
Figure 3: Shot 20057, the ToA signal from the Timepix3 plotted with the key diagnostics from the tokamak. The Ar puff is shown in orange. The Timepix3 operated with ≈ 1600 pixels active.

Figure 4: Shot 20059, the ToA signal from the Timepix3 plotted with the key diagnostics from the tokamak. The Ar puff is shown in orange. The Timepix3 operated with ≈ 1600 pixels active.
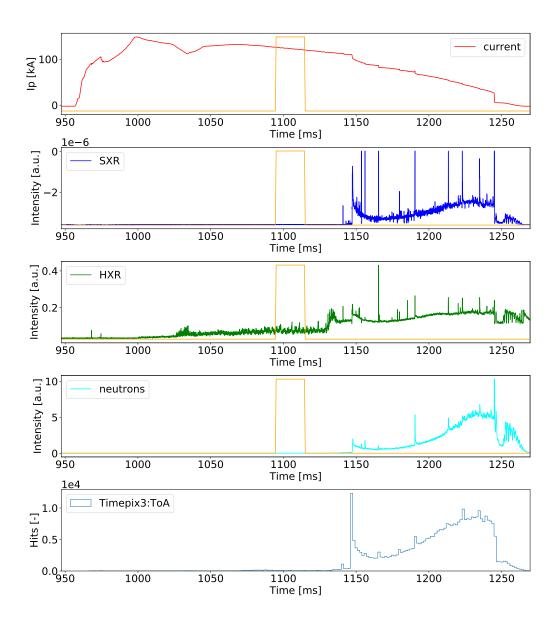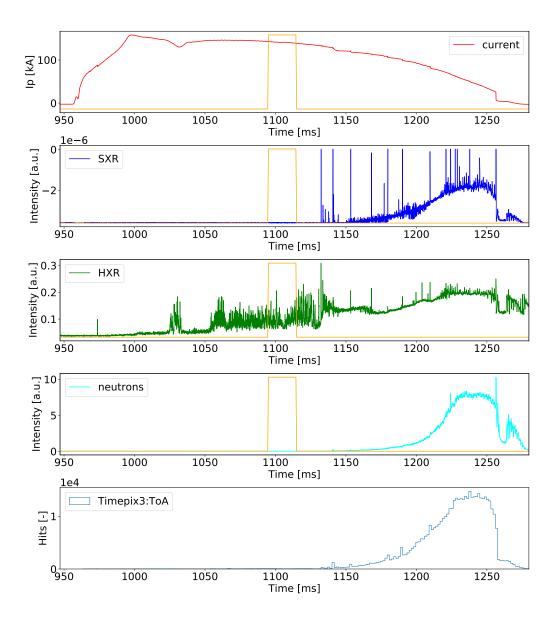
Figure 5: Shot 20062, the ToA signal from the Timepix3 plotted with the key diagnostics from the tokamak. The Ar puff is shown in orange. The Timepix3 operated with ≈ 1600 pixels active.

Figure 6: Shot 20065, the ToA signal from the Timepix3 plotted with the key diagnostics from the tokamak. The Ar puff is shown in orange. The Timepix3 operated with ≈ 1600 pixels active.
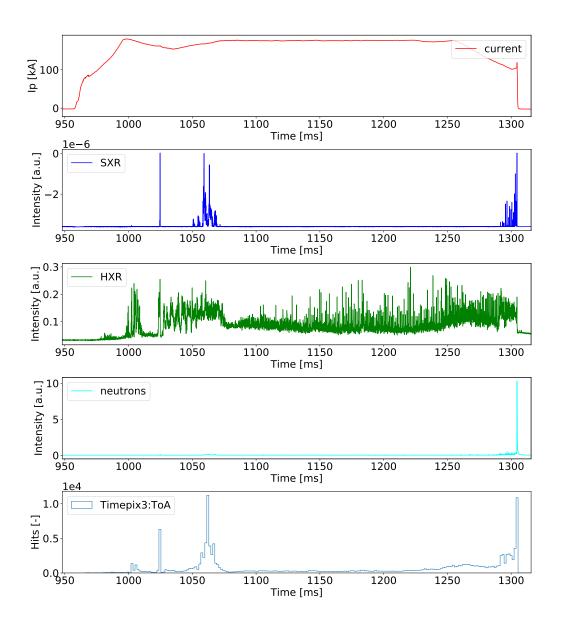
Figure 7: Shot 20070, the ToA signal from the Timepix3 plotted with the key diagnostics from the tokamak. The shot was conducted without any impurity gas puff. The Timepix3 operated with ≈ 12000 pixels active.
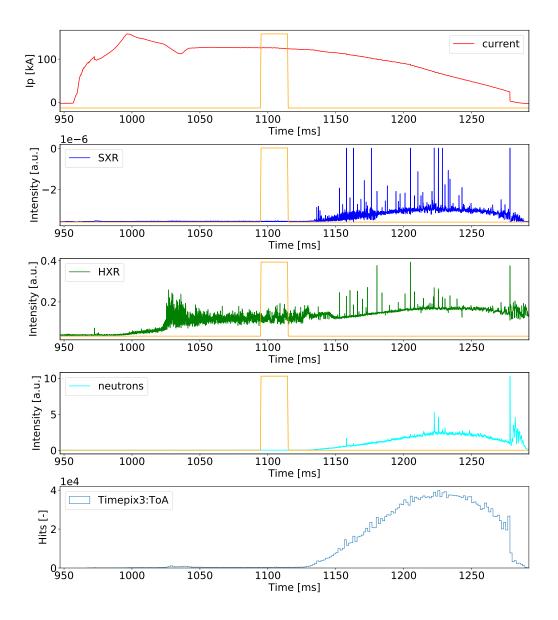
Figure 8: Shot 20075, the ToA signal from the Timepix3 plotted with the key diagnostics from the tokamak. The Ar puff is shotn in orange. The Timepix3 operated with ≈ 12000 pixels active.